

Activity of TRAPPIST–1 analogue stars observed with *TESS*

Bálint Seli^{1,2}, Krisztián Vida¹, Attila Moór¹, András Pál¹, and Katalin Oláh¹

¹ Konkoly Observatory, Research Centre for Astronomy and Earth Sciences, H-1121 Budapest, Konkoly Thege M. út 15-17, Hungary

² Eötvös University, Department of Astronomy, Pf. 32, 1518 Budapest, Hungary

Received December 9, 2020

ABSTRACT

As more exoplanets are being discovered around ultracool dwarfs, understanding their magnetic activity – and the implications for habitability – is of prime importance. To find stellar flares and photometric signatures related to starspots, continuous monitoring is necessary, which can be achieved with spaceborn observatories like the Transiting Exoplanet Survey Satellite (*TESS*).

We present an analysis of TRAPPIST–1 like ultracool dwarfs with *TESS* full-frame image photometry from the first two years of the primary mission. A volume-limited sample up to 50 pc is constructed consisting of 339 stars closer than 0^m5 to TRAPPIST–1 on the *Gaia* colour–magnitude diagram. The 30-min cadence *TESS* light curves of 248 stars were analysed, searching for flares and rotational modulation caused by starspots. The composite flare frequency distribution of the 94 identified flares shows a power law index similar to TRAPPIST–1, and contains flares up to $E_{TESS} = 3 \times 10^{33}$ erg. Rotational periods shorter than 5^d were determined for 42 stars, sampling the regime of fast rotators. The ages of 88 stars from the sample were estimated using kinematic information. A weak correlation between rotational period and age is observed, which is consistent with magnetic braking.

Key words. Stars: activity – Stars: flare – Stars: late-type – Stars: low-mass – (Stars:) starspots – Stars: statistics

1. Introduction

Low-mass, cool M-dwarfs are the prime targets when searching for exoplanets. One appealing trait of these objects is that their habitable zone is much closer to an M-dwarf host than to a solar-like star, thus detecting a possibly habitable Earth-like planet is easier. Currently there are about 4000 known exoplanets, but interestingly only very few of these were found around ultracool dwarfs (UCDs, late M dwarfs and brown dwarfs). One of these is Proxima Centauri (M5.5 V) – the closest star to the Sun – that hosts an Earth-mass planet in its habitable zone (Anglada-Escudé et al. 2016). The other one is Teegarden’s star (2MASS J02530084+1652532; M7V), where Zechmeister et al. (2019) recently reported two Earth-mass planets, that are among the lowest-mass planets discovered so far. The third example is TRAPPIST-1 (2MASS J23062928-0502285; *Gaia* DR2 2635476908753563008; M8V), that is known to host seven transiting exoplanets, three of which have equilibrium temperatures that makes the existence of liquid water on their surface possible (Gillon et al. 2017). However, due to the low luminosity of these objects in the optical regime, obtaining high signal-to-noise photometric or spectroscopic observation is challenging, hence the low number of currently known exoplanets around UCDs.

The habitability of the planets hosted by UCDs is in the focus of intense debates, as a large fraction of them is magnetically active, producing e.g. frequent flares. These can damage the atmospheres of the orbiting planets by changing the atmospheric composition or completely eroding the atmosphere over time (see Vida et al. 2017; Roettenbacher & Kane 2017; Vida et al. 2019b; Glazier et al. 2020, and references therein). On the other hand these events can be the source of the UV radiation needed for abiogenesis (Ranjan et al. 2017). On our Sun a large fraction of the flares are accompanied by coronal mass ejections (CMEs), that also can have deleterious effects on planetary atmospheres. However, observations suggest that while the detected

CMEs are more frequent on the later-type, more active UCDs, most of these events are unsuccessful eruptions, with velocities below the escape velocity (Vida et al. 2016, 2019a). This is further confirmed by magnetohydrodynamic simulations, that suggests that only the largest eruptions might be able to escape from the strong magnetic field of these stars (Alvarado-Gómez et al. 2018).

To understand these systems, long-term observations would be optimal. However, in this paper we chose a different approach: instead of observing a single target for an extended period of time, we aim to gain statistical knowledge of the flaring activity based on the photometry of many similar stars. To this end, we choose TRAPPIST–1 as the main target, and compile a list of similar objects we call *TRAPPIST–1 analogues*. As a measure of similarity we simply use the distance between stars on the *Gaia* colour–magnitude diagram, and adopt a lower limit on parallax to have a volume-limited sample. As for the photometric observation, we use data provided by the *Transiting Exoplanet Survey Satellite* mission (*TESS*; Ricker et al. 2015). *TESS* performed its primary mission between July 2018 and July 2020, covering the majority of the sky divided into observation runs called *sectors*. One sector covers 24×96 degrees in a nearly continuous field-of-view (FoV), assembled from the 24×24 degree FoVs of four individual identical cameras lined up to provide the final geometry. The two years of the primary mission were divided into a Southern Survey (1st year) and Northern Survey (2nd year), where each of the corresponding 2×13 sectors were observed for approximately one sidereal month (~ 27.3^d). The sectors were arranged in a way to provide overlaps and therefore nearly continuous observations for a year at the vicinity of the ecliptic poles¹. *TESS* images are available for the entire FoV with 30-min cadence, while a limited number of stars are observed with 2-min cadence. To make our analysis homoge-

¹ <https://tess.mit.edu/observations/>

neous, we only use the 30-min full-frame images (FFIs), which are available for $\sim 3/4$ of virtually any spatially homogeneous stellar sample (in the two years of the *TESS* primary mission, which avoids the ecliptic). Our primary objective is to detect the rare high energy flares, and many studies have shown that it is possible with this relatively long cadence (see e.g. Davenport 2016; Van Doorselaere et al. 2017). This cadence is also sufficient for the detection of photometric rotational period of UCDs in the order of a few days.

The structure of the paper is as follows: we define the TRAPPIST-1 analogue sample in Sect. 2, then in Sect. 3 the analysis of the *TESS* light curves is presented, including period search and flare identification. In this section we also look for $H\alpha$ emission in publicly available optical spectra, and compile the approximate ages of stars in the sample. We then discuss the implications of our findings in Sect. 4, regarding the period distribution, flare rate and possible correlations. Finally the main results are summarised in Sect. 5.

2. Sample selection

Since TRAPPIST-1 lies near the ecliptic, *TESS* did not observe it in the first two years of the primary mission, and the next opportunity will be during the fourth year, when Sectors 42–46 will be centered on the ecliptic. So to study UCDs like TRAPPIST-1, we selected similar stars (henceforth TRAPPIST-1 analogues) based on simple photometric criteria. The selected stars need to be closer than 0^m5 to TRAPPIST-1 on the *Gaia* ($G_{BP} - G_{RP}$) – M_G diagram (see Fig. 1). This results in a circle around TRAPPIST-1, which has the following parameters: $G_{BP} - G_{RP} = 4.^m901 \pm 0.^m049$, $M_G = 15.^m1728 \pm 0.^m0035$. To get a volume limited sample for homogeneous analysis, only stars closer than 50 pc were considered. Limiting our search to nearby stars is also practical so our sample will contain only targets within the reach of *TESS*. According to TICgen², TRAPPIST-1 at 50 pc would be $\sim 17^m$ in the *TESS* bandpass with photometric error around $0.^m07$ on 30-min exposures, enough to detect the highest energy flares. This value agrees with the pure *Gaia* DR2-based estimation of $17.^m10$. Such an estimation is rather accurate due to the nearly perfect overlap of the bandpasses of the *TESS* cameras and the *Gaia* G_{RP} colour (see Fig. 3 in Jordi et al. 2010).

We used a custom query (Table 1) on the *Gaia* TAP (Table Access Protocol) server³ to obtain the set of stars with reliable observations within 50 pc. The flux error limits employed in this query were based on the work of Reylé (2018). The last line of the query corresponds to the Renormalised Unit Weight Error (RUWE), retaining sources with well-behaved astrometric solutions. Since the stars of interest are in the solar neighbourhood, reddening and interstellar extinction were not taken into account.

After applying our photometric criteria on this list 271 stars remained, with 144 also present in the UCD catalogue of Reylé (2018). To complement this list with known UCDs (since e.g. TRAPPIST-1 itself was excluded by RUWE), we also added stars from the *List of M6-M9 Dwarfs*⁴ curated by J. Gagné, disregarding the quality criteria used in the previous *Gaia* query. Also we included 36 new stars from the volume-limited *Ultra-cool SpeXtoscopic Survey* of Bardalez Gagliuffi et al. (2019) in the same manner. All the added stars are within 50 pc and inside the $0.^m5$ circle on the *Gaia* colour–magnitude diagram, their exclusion from the original sample was due to either

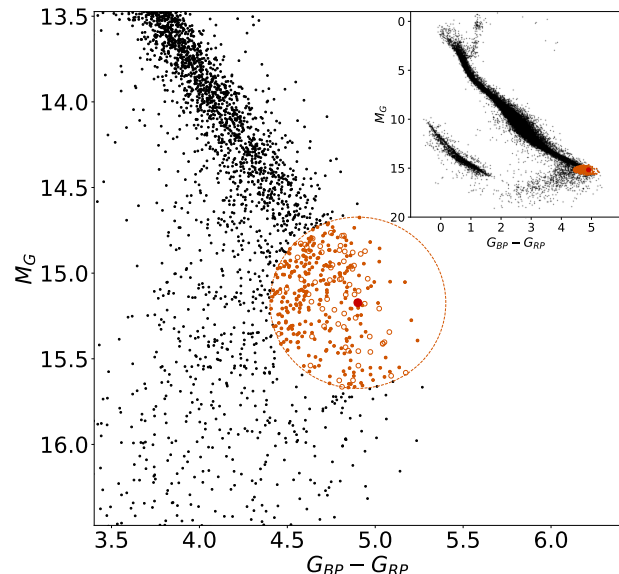


Fig. 1. Selection criteria on the *Gaia* colour–magnitude diagram. Red point shows the position of TRAPPIST-1, orange points represent the final TRAPPIST-1 analogue sample. Empty orange circles indicate stars that were not initially included due to the *Gaia* quality cuts, but were later added from existing UCD catalogues.

$visibility_periods_used \leq 8$ or RUWE. The final sample consists of 339 targets, summarised in Table 2. Propagating the *Gaia* uncertainties of TRAPPIST-1 to the selection, the scatter in the sample size is ± 39 . As a sanity check we queried the Simbad database with the *Gaia* DR2 identifiers, and $\sim 90\%$ of the valid spectral types were indeed between M7 and M9. We note that while the *Gaia* EDR3 is now available, it could add only a few UCD candidates to the sample. According to Gaia Collaboration et al. (2020), the number of new UCDs up to 100 pc is 1016 objects, most of them in the faint regime that can not be reliably observed with *TESS*.

The brightness distribution of our sample can be seen in Fig. 2. Since the *Gaia* G_{RP} bandpass is similar to the *TESS* bandpass, we expect most targets to be brighter than $T = 17^m$. Fig. 3 shows the position of the targets with equal-area Aitoff projection. Open circles indicate stars that were not observed in the *TESS* primary mission, mostly due to the exclusion of the ecliptic.

325 stars from the sample had entry in the *TESS* Input Catalog (TICv8, Stassun et al. 2019), with the following median parameters: $\log g = 5.27 \pm 0.01$, $M = 0.092 \pm 0.003 M_{\odot}$, $L = 0.0007 \pm 0.0004 L_{\odot}$, $R = 0.116 \pm 0.003 R_{\odot}$. While there are no effective temperature measurements below 2700 K in TICv8, there is a generally good agreement of the other parameters compared to Gonzales et al. (2019). 70 stars from the sample have temperature measurement in *Gaia* DR2, with 3318 ± 23 K median value, while TRAPPIST-1 itself has 3352^{+104}_{-62} K. However, the *Gaia* temperatures are not reliable in this regime, since the algorithm was trained on stars hotter than 3000 K, and there is a degeneracy between temperature and extinction/reddening (Gaia Collaboration et al. 2018).

² <https://github.com/tessgi/ticgen>

³ <http://gea.esac.esa.int/tap-server/tap>

⁴ <https://jgagneastro.com/list-of-m6-m9-dwarfs/>

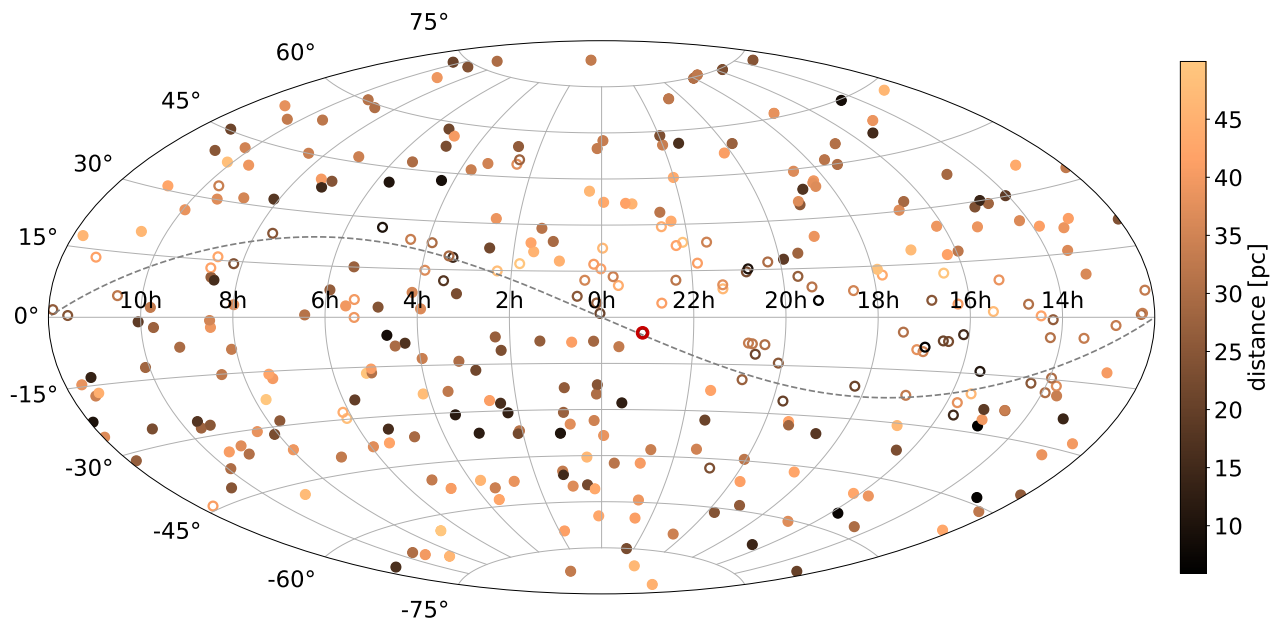


Fig. 3. Position of the selected stars on the sky with equatorial coordinates, colour coded with distance. Stars plotted with filled points have been observed by *TESS* up to Sector 26. Red circle represents TRAPPIST-1. The ecliptic is shown with dashed line for reference.

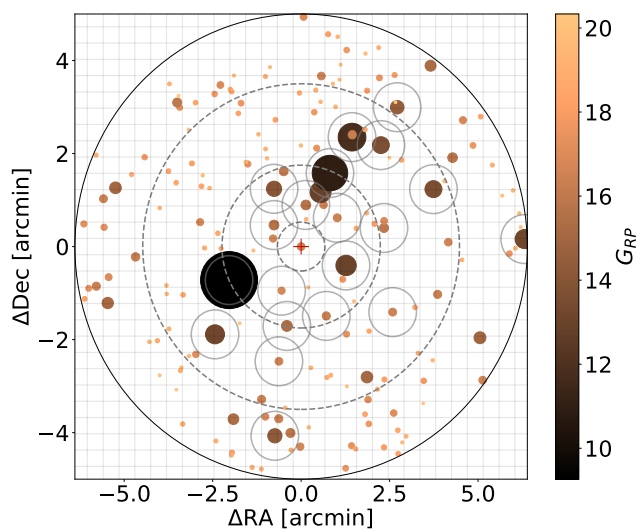


Fig. 4. The field of view of a selected target (Gaia DR2 2883680659313632896) from *Gaia*, with 173 stars brighter than 20^m . Red cross marks the target, dashed circles show the aperture and annulus used for the *TESS* photometry, and solid circles show the stars selected for PCA. The grid in the background illustrates the pixel scale of *TESS*.

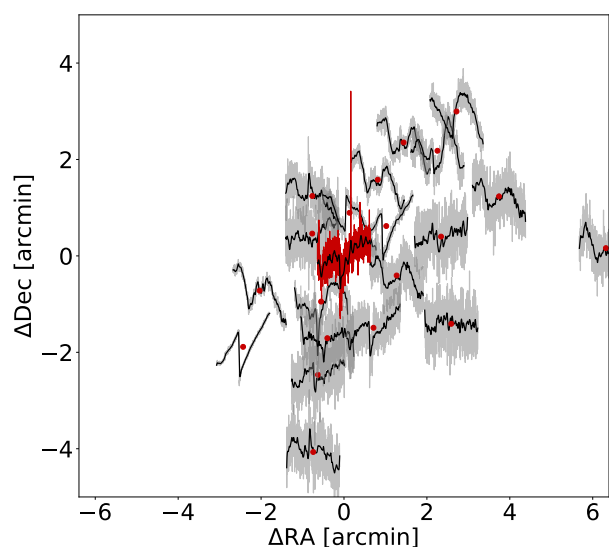


Fig. 5. Extracted light curves from the circular apertures of Fig. 4, with red dots indicating the celestial position of the sources. Some common trends can be identified, while the large flare seen on the target (red curve) does not seem to appear anywhere else.

for PCA were interpolated to the time values of the main target, so that all datasets contain the same number of points. We also tried the same approach with flux instead of magnitude, but the results were essentially the same. A light curve containing periodic variation and a flare event can be seen in Fig. 6.

3.2. Period search

Ultracool dwarfs often have rotational periods less than a few days, therefore even one 27^d long *TESS* sector could be enough

to detect the rotational modulation caused by starspots. To search for rotational periods, we inspected the Lomb–Scargle periodogram (Lomb 1976; Scargle 1982) of all stars in the observed sample (248 stars out of 339, with 370 light curves). To make the analysis homogeneous, the periodograms were plotted for each sector separately, and only periods shorter than 5^d were considered (similar to Medina et al. 2020 or Günther et al. 2020). Several targets showed Lomb–Scargle peaks longer than 5^d , but the strong contamination and short temporal baseline would make these detections ambiguous.

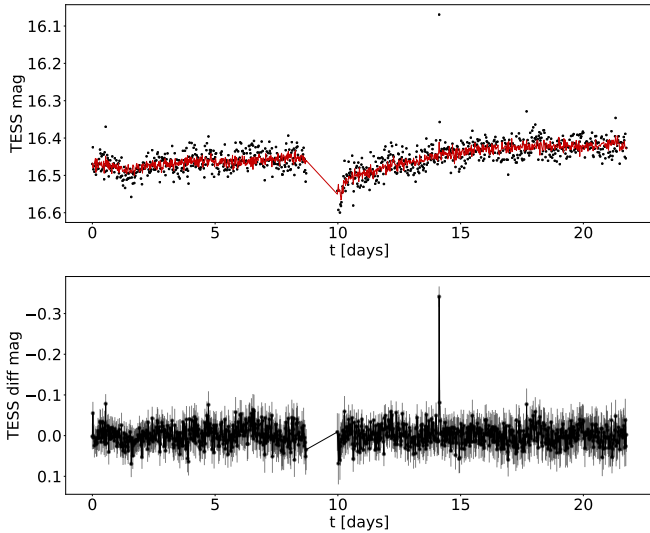


Fig. 6. PCA reconstruction of the light curve from Fig. 5. Black points on the upper panel show the light curve created by `QDLP_EXTRACT`, red curve shows the PCA reconstruction. The corrected light curve can be seen on the lower panel, with a dominant flare and periodic variation.

After clipping the outliers from the light curve with 3σ threshold, the Lomb–Scargle periodogram was plotted, and the 5 largest peaks were identified between 1.5 hours and 5^d . We folded the light curves with these trial periods, and inspected the results manually. Since all the stars with detected period showed simple sinusoidal variation, only one Fourier term was used for the analysis.

To assess the significance of the periodogram peaks, the False Alarm Probability (FAP) was calculated. The FAP quantifies the probability that a peak with the given height is observed from Gaussian noise alone, purely by chance. We note that a FAP value close to zero does not mean that the given period is the correct one. Only peaks with FAP less than 1% were considered.

To calculate the uncertainty of the peak position, we took the best fitting sinusoidal model, and created 1000 realisations adding Gaussian noise with the scatter of the residual light curve. The period analysis was repeated, and the position of the largest peak was saved. The uncertainty of the period was then calculated as the standard deviation of these periods. We note that this uncertainty generally scales with the value of the period itself, increasing for longer periods.

Most of the stars with detected period show simple sinusoidal light curves, possibly due to the relatively long cadence compared to the short rotational periods. If these stars would show complex rotational modulation (e.g. as in Zhan et al. 2019), the 30-min integration time would blur the sharp features. The distribution of the detected rotational periods is plotted in Fig. 8. We return to its discussion in Sect. 4.

3.3. Flares

Flares appear as sudden brightening of the stellar atmosphere that occur when the magnetic field lines reconnect, and a portion of magnetic energy is released. Their usual timescale is minutes to hours. Even though white-light flares are rarely observed on the Sun, they are quite common on later-type stars (see e.g. Namekata et al. 2017). Apart from the rotational modulation caused by starspots, flares are the most easily observable mani-

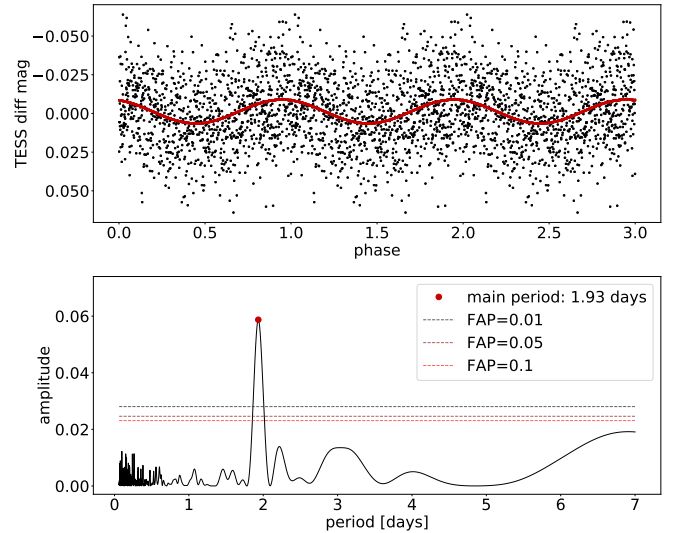


Fig. 7. Period analysis for the corrected light curve from Fig. 6. Upper panel shows the light curve phase folded with the 1.93^d period, which can be identified on the Lomb–Scargle periodogram below.

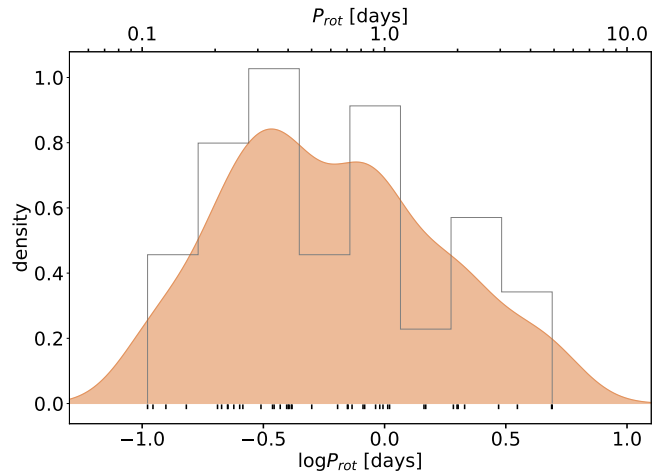


Fig. 8. Rotational period distribution of the sample with *TESS*. The one-dimensional kernel density estimation plotted with orange is calculated with a Gaussian kernel with bandwidth of 0.15. The black ticks show the individual period values. We note that due to the 27^d baseline of *TESS* sectors, only periods below 5^d were kept.

festation of magnetic activity in optical light curves. So to characterize the activity of TRAPPIST-1 analogues, we searched for flares on the 30-min *TESS* light curves.

Due to the high noise level of the light curves, we chose to identify flares manually. We selected events with at least two consecutive outlying points (with at least one point exceeding twice the local scatter), resulting in 94 detections. These flares were found on 21 stars, all with detected rotational period, which means that 50% of the fast rotators in our sample show flares (similar to the $\sim 60\%$ found by Günther et al. 2020).

To characterise the flares, we calculated the equivalent duration (ED, Gershberg 1972), i.e. the integrated area under the flare curve (the time needed for the quiescent star to radiate the same amount of energy that was released during the flare event). The total energy output of an event can be calculated by multiplying this value with the quiescent luminosity of the star. We converted

the light curves to flux, and ran the full detrending procedure, which involves normalising by the median value, then subtracting the PCA reconstruction, resulting in dimensionless flux centered on zero. We then iteratively σ -clipped points with lower and upper rejection threshold of 3σ and 2σ , respectively, which effectively removed the flares. We then smoothed the remaining dataset with a LOWESS filter (Locally Weighted Linear Regression, Cleveland 1979) with Gaussian kernel width of 0.06^d . This smoothed dataset was then interpolated onto the time frame of the original light curve, and subtracted from it. This step removed the variation induced by starspots. We calculated the ED on these light curves employing two different approaches. First, we simply integrated the area of the flares using the trapezoidal rule. To estimate the uncertainty of this method, we re-sampled the light curve using the flux values and error bars as the mean and scatter of a Gaussian distribution. We generated 1000 such realisation of the light curve, calculated the ED again, and took the standard deviation.

As a second approach, we fitted the flares with the single-peaked empirical template of Davenport et al. (2014), parameterized by the t_{peak} time of the peak, A amplitude and $t_{1/2}$ width of the flare. After transforming the measured time t to $t' = \frac{t-t_{\text{peak}}}{t_{1/2}}$, the flare template function is given by:

$$\begin{cases} 0 & \text{if } t' < -1 \\ A \cdot (1 + 1.941t' - 0.175t'^2 - 2.246t'^3 - 1.125t'^4) & \text{if } -1 \leq t' < 0 \\ A \cdot (0.6890e^{-1.600t'} + 0.303e^{-0.2783t'}) & \text{if } 0 \leq t' \end{cases} \quad (1)$$

To fit the observations we used the Markov Chain Monte Carlo (MCMC) implementation of `PyMC` (Fonnesbeck et al. 2015) with uniform prior around an approximate t_{guess} on t_{peak} , and exponential priors on A and $t_{1/2}$, where λ is the parameter of the exponential distribution:

$$t_{\text{peak}} \sim \mathcal{U}(t_{\text{guess}} - 1^d, t_{\text{guess}} + 1^d) \quad (2)$$

$$A \sim \text{Exp}(1/\lambda = 0.4) \quad (3)$$

$$t_{1/2} \sim \text{Exp}(1/\lambda = 0.2^d) \quad (4)$$

We run the MCMC chains starting from the maximum a posteriori value for 100 000 steps, discarding the first 20 000 steps as burn-in and only leaving every second step as thinning. A successful fit can be seen in Fig. 9 (following the example of Fig. 6), while for a few smaller flares the MCMC chain did not converge (13 of the 94 flare events, see Table B.1). The fits generally overestimated the flare amplitudes (see Fig. 10), and hence the EDs, but they give a reliable estimate of $t_{1/2}$ even for shorter events. A similar behaviour was observed by Raetz et al. (2020), where the amplitudes were systematically higher using *Kepler* short cadence light curve compared to long cadence. We experimented with fitting only two parameters, after forcing the fitted ED to be equal to the previously calculated one, but essentially the same behaviour was observed. According to Fig. 11, the flare EDs mainly scale with the amplitude, and there is no dependence on $t_{1/2}$.

The ED of the 94 flare events were converted to energy by multiplying by the quiescent stellar luminosity. Since the sample consists of stars similar to TRAPPIST-1, we simply

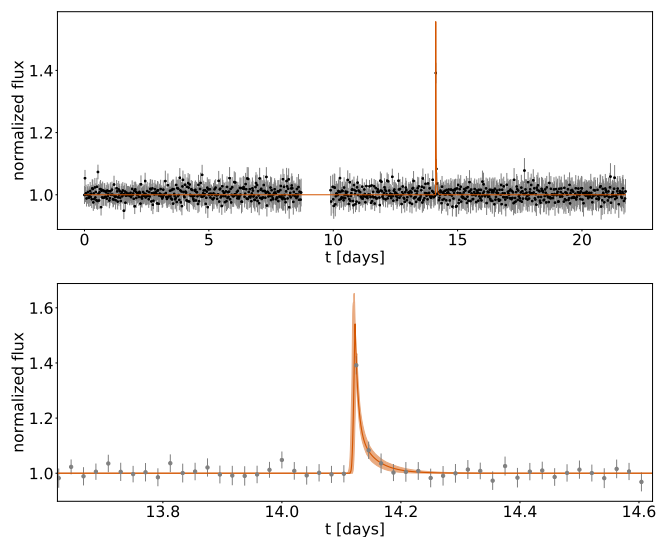


Fig. 9. A flare event fitted with the analytical template following the example of Fig. 6. The summed ED is 15.4 ± 2.9 min, while the fit gives 12.9 ± 4.4 min.

used its luminosity for all targets. It was calculated by convolving the *TESS* response function⁶ with a BT-NextGen model spectrum ($T_{\text{eff}} = 2600$ K, $\log g = 5.0$, $[\text{Fe}/\text{H}] = 0$), scaling with the $L_{\text{bol}} = 0.00061 \pm 0.00002 L_{\odot}$ bolometric luminosity of TRAPPIST-1 from Gonzales et al. (2019). The estimated luminosity of TRAPPIST-1 in the *TESS* bandpass is thus $L_{\text{TESS}} = (2.1 \pm 0.3) \times 10^{29}$ erg s⁻¹, with nominal uncertainty calculated using models with ± 100 K temperature. Using a simple black body spectrum with the same temperature would give 2.9×10^{29} erg s⁻¹. Integrating the same BT-NextGen model spectrum gives $L_{\text{Kepler}} = (5.6 \pm 1.5) \times 10^{28}$ erg s⁻¹ for the luminosity in the *Kepler* bandpass. Compared to the nominal errors cited here, the dominating source of uncertainty is the different luminosities within the sample itself, since M_G varies by $\pm 0.5^m$.

As a validation of the temperature and luminosity used above, Gonzales et al. (2019) lists 4 field dwarfs similar to TRAPPIST-1, with 2603 K and $0.00058 L_{\odot}$ mean temperature and luminosity in their Table 3, plotted in their Fig. 2a. These 4 stars are also present in our sample, and LHS 132 (Gaia DR2 4989399774745144448) and LHS 3003 (Gaia DR2 6224387727748521344) have already been observed by *TESS*.

3.3.1. Feasibility check with downgraded *Kepler* K2 data

To demonstrate the viability of this project, we converted real photometric observations of TRAPPIST-1 to match the quality of a *TESS* FFI dataset. We took the *Kepler* K2 short cadence light curve of Vida et al. (2017), converted it from magnitude to flux, scaled up the noise level by a factor of 10 (ratio of the *Kepler* and *TESS* apertures), and rebinned it from 1 to 30-min cadence. We then inspected the resulting light curve (Fig. 12), and identified flare events passing the same criteria as the TRAPPIST-1 analogues. While the original light curve showed 42 distinguishable flares, from the downgraded light curve we could only identify 8 of them, only those with the highest energies. However, the energy estimates agreed within the nominal uncertainties. We note that some of the larger flares remained as a single outlier point,

⁶ <https://heasarc.gsfc.nasa.gov/docs/tess/data/tess-response-function-v2.0.csv>

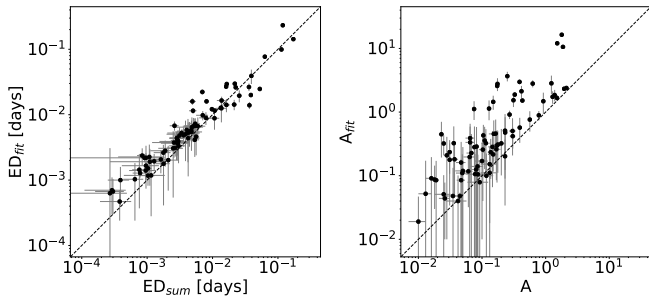


Fig. 10. *Left:* Comparison of the summed and fitted EDs. While they generally give the same result, they can differ by a factor of 2–3. *Right:* Comparison of the observed flare amplitude (the highest flux value) and the fitted amplitude. Due to the low time resolution, the observed peak is generally smaller.

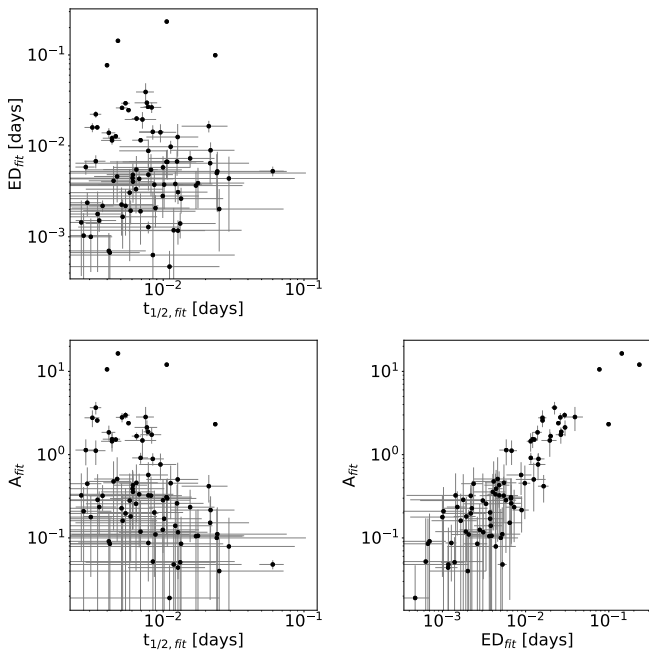


Fig. 11. Correlations between the flare parameters.

but in real observations we could not safely label such events as flares, so we omitted them here as well. It appears that flares with energies above $\sim 10^{31}$ erg can be observed even with the 10 cm aperture of *TESS*, on a $T \sim 14^m$ star.

3.3.2. Completeness

Less energetic flares are harder to distinguish from noise, so they are easily missed. To de-bias the flare frequency distribution (FFD) from this selection effect, we calculate the flare recovery rate (hereafter called completeness) for each light curve, for given flare energies. To do this, we inject artificial flare signals into the light curves, and try to recover them.

Each of the light curves were converted to flux, and clipped with a 3σ threshold. The clipped values were then linearly interpolated to fill the gaps induced by real flare events. Next, we added artificial flares with different EDs. To generate a flare with the given ED, t_{peak} was drawn from the observed time interval, $t_{1/2}$ was drawn uniformly from 0.001^d to 0.05^d , and the ampli-

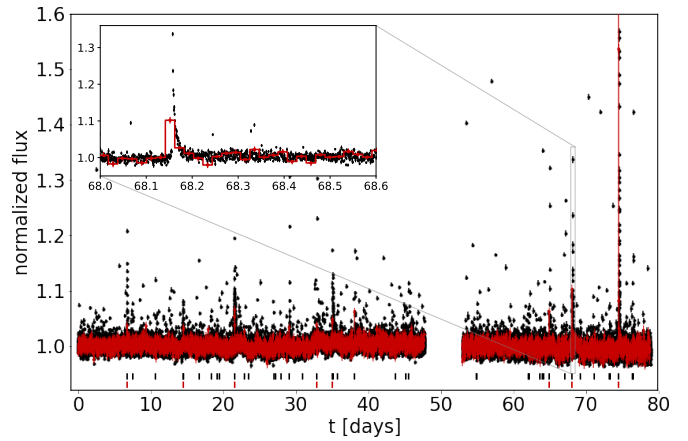


Fig. 12. The *Kepler* K2 light curve of TRAPPIST-1 from Vida et al. (2017) (black) rebinned to 30-min time resolution, and with *TESS*-like scatter (red). Black and red ticks below the light curve indicate the position of flares found in the corresponding dataset.

tude of the flare was scaled to match the required ED. Next, the local scatter was calculated in a 4^d long interval, and the light curve was smoothed with a 0.2^d wide LOWESS kernel. A flare is considered to be detected if a point is twice the scatter above the smoothed light curve, with the following point still exceeding once the scatter. This criterion was chosen to match visual inspection. For each light curve, 100 ED bins were defined logarithmically from 10 to 10^4 s, and 100 random flares were generated for each ED. The completeness is defined as the fraction of recovered flares.

Taking the multiplicative inverse of the completeness value for each detected flare energy, the FFD calculated from a single light curve can be corrected. However, most of the flares in our sample come from different stars with different photometric noise properties, i.e. with different completeness curves. In order to correct the composite FFD of the whole sample, a single representative correction curve is needed. For this purpose we simply average the completeness curves calculated from each individual light curve. As it can be seen in Fig. 13, this approach is equivalent to a completeness curve calculated from all the light curves concatenated into a single dataset, spanning ~ 23 years. The uncertainty is calculated from the 84th and 16th percentiles of all the single-sector completeness curves. We note that for lower energies even a small difference in the recovery rate can result in a large difference in the composite FFD, thus the lower energy part should be treated with caution. Normally, when a similar approach is used, the difference between the original and corrected FFD is only a few percent. We also note that this method is not strictly correct, as we identified flares manually without a rigorous detection algorithm, since the high noise level of the light curves did not allow us to use one.

The same method was also used to calculate the flare recovery rate for the K2 short cadence light curve of TRAPPIST-1 from Vida et al. (2017).

The reliability of the ED estimation method was also tested in a similar manner, by injecting artificial flares into the light curves. Due to the high photometric noise, the measured differences in ED can exceed the nominal uncertainties. For flares above $E_{\text{TESS}} = 10^{32}$ erg, the measured EDs were erroneous by a factor of 10 in $\sim 5\%$ of the injected flares. However, the differences are not expected to be this severe for most of the detected

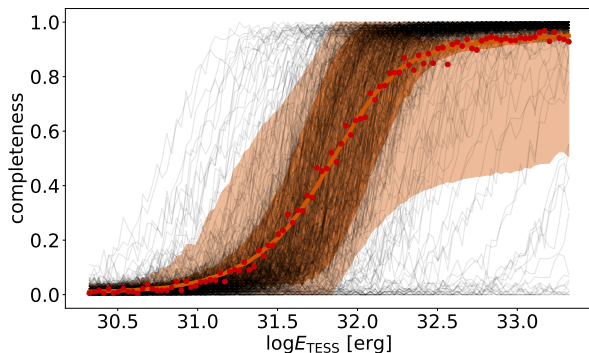


Fig. 13. Flare recovery rate calculated for each light curve. The orange line shows the average curve for all stars, red points show the completeness curve calculated for a concatenated light curve. The shaded regions show the 1 and 2 σ confidence intervals.

events, since we have used all light curves – even the noisiest ones – for the injection tests.

3.4. H α emission

To look for emission features, we checked the *Rizzo Spectral Library*. 95 stars from our sample had available optical spectra, published by Cruz et al. (2003), Cruz et al. (2007) and Reid et al. (2008). The average wavelength range of these spectra is from 5600 Å to 10000 Å, with average $\frac{\lambda}{\Delta\lambda}$ resolution between 2000 and 5000. Most stars showed prominent emission in H α . We calculated the H α equivalent width (EW) by integrating the flux between 6553 and 6573 Å, after normalising by a linear fit to the local continuum. The uncertainty of the EW was estimated by re-sampling from the flux errors. We note that the flux errorbars were generally larger in the vicinity of H α if the emission was stronger, leading to high (and possibly overestimated) uncertainties even for high EW values. The measured EWs are listed in Table 2.

3.5. Age determination

To see how the activity signatures evolve, it would be interesting to have an age estimation for as many stars from the sample as possible. While TRAPPIST-1 itself is fairly old (7.6 ± 2.2 Gyr, Burgasser & Mamajek 2017), the sample discussed here should include objects with different ages, since these low-mass objects move on the Hertzsprung–Russell diagram slowly during their evolution, while the selection criteria were related to colour and luminosity alone. Unfortunately, all the other parameters of these stars evolve slowly with age, making the inference troublesome. In this section we explore the available methods to estimate stellar ages in this low-mass regime.

While the ages of individual objects are hard to estimate, it is not the case for clusters and moving groups. With available astrometric information the probability that these stars are members of known moving groups can be estimated. To this end, we utilized BANYAN Σ (Gagné et al. 2018). It can predict membership probabilities for 27 young associations within 150 pc, using position and velocity information. No stars in the sample had measured radial velocity in *Gaia* DR2, but 72 of them had literature measurements in the Simbad database. For these stars all 6-dimensional position and velocity information was used, while the radial velocity was omitted for the

remaining objects. 14 stars had membership probability over 95%. *Gaia* DR2 65638443294980224, 3200303384927512960, 4900323420040865792 and 89186168428165632 had high membership probability and confirmation from the literature (Goldman et al. (2013), Baron et al. (2019), Gagné et al. (2015) and Bardalez Gagliuffi et al. (2019), respectively). Burgasser et al. (2015) have found that *Gaia* DR2 6224387727748521344 does not show signs of young age, so it was rejected as an AB Doradus member. Although the remaining stars have no confirmation of young age from the literature nor measured radial velocity, they were kept as candidate moving group members.

For those 72 stars that had radial velocity measurements the full 6-dimensional position and velocity information is available. This lends itself to kinematic age estimation, a method that uses the motion within the galactic disk as a proxy for age. Young objects tend to have simple orbits with smaller peculiar velocities, while older stars are scattered to more eccentric and inclined orbits. We used the method of Almeida-Fernandes & Rocha-Pinto (2018) to calculate the age probability density function (PDF) from the UVW galactic velocity components. The method is calibrated using isochronal ages of $\sim 14\,000$ stars from the Geneva–Copenhagen Survey. While most of the other methods (like isochrone fitting) is not applicable to low-mass stars, there is no mass dependency in the kinematic method. As a downside, the precision is low (the 1 σ errorbars are typically 2–3 Gyr).

First we converted the *Gaia* DR2 position, proper motion, parallax and literature radial velocity data to galactic velocity components. The measurement uncertainties were propagated into the UVW components by re-sampling the input values. We then used the "UVW method" described in Sect. 3.1 of Almeida-Fernandes & Rocha-Pinto (2018), by calculating the components of the velocity ellipsoid, and building the age PDF as a product of 3 Gaussians. To extract a point estimate from the PDF, we calculated the most likely age (t_{ML}) as the mode of the distribution, and the expected age (t_E) as

$$t_E = \int_0^{13.8 \text{ Gyr}} t p(t|U, V, W) dt \quad (5)$$

where $p(t|U, V, W)$ is the age PDF calculated numerically between 0 and 13.8 Gyr. Following the suggestions of Almeida-Fernandes & Rocha-Pinto (2018), we used the following kinematic age as the estimated value:

$$t_{kin} = \frac{3t_{ML} + t_E}{4} \quad (6)$$

with the uncertainty of

$$\delta_t = \frac{1}{4} \left[(t_{84} - t_{16}) + \frac{t_{97.5} - t_{2.5}}{2} \right] \quad (7)$$

where the subscripts of t denote percentiles. In the case of Gaussian distribution δ_t corresponds to 1 σ . To take the measurement uncertainty of the UVW components into account, 100 realizations of the PDF were calculated using re-sampled UVW values, and the point estimates were calculated from the median PDF. We also chose to add the scatter in the 100 individual t_{kin} values in quadrature to δ_t , which generally increased δ_t by ~ 0.1 Gyr. To illustrate the method, an example PDF can be seen in Fig. 14.

An other technique to determine ages of UCDs is to look for wide binary pairs, where the age of the other component can be measured (assuming coevality). For all stars in the sample, we queried *Gaia* DR2 looking for stars with similar astrometric parameters. For this we utilized the same criteria as proposed by Smart et al. (2019), except that our search was limited to

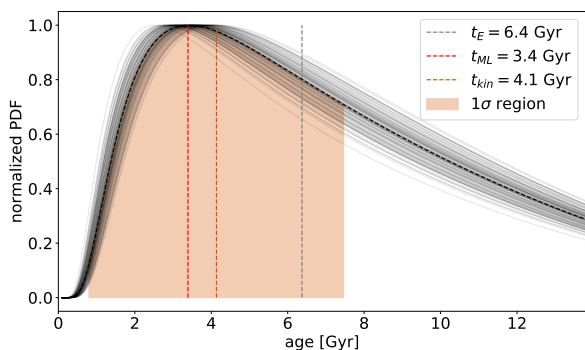


Fig. 14. The kinematic age PDF of *Gaia* DR2 3421840993510952192, with $(U, V, W) = (33.0 \pm 4.0, -20.5 \pm 0.2, -22.2 \pm 0.5)$ km s⁻¹. Thin black lines show 100 realizations of the PDF taking into account measurement errors.

a projected separation of 0.2 pc. This resulted in 19 comoving pair candidates, with 0.05 pc maximum separation, summarised in Table C.1. Radial velocity measurement was available for 9 stars, making kinematic age estimation possible.

Out of these 19 stars, *Gaia* DR2 1412377317863375488 has measured rotational period, but no kinematic age estimate. Its comoving pair is HD 234344, a bright K3 dwarf with measured radial velocity from *Gaia* DR2. The kinematic method gives 3.7 ± 3.3 Gyr, while isochrone fitting combined with gyrochronology with *STARDATE* (Angus et al. 2019) gives $0.1^{+2.4}_{-0.1}$ Gyr (using the peak of the age posterior). We used $3.1853^d \pm 0.004^d$ rotational period measured from 3 sectors of *TESS* FFI data.

As an independent means of age estimation, we inspected all the available optical spectra from the *Rizzo Spectral Library* looking for lithium absorption around 6708 Å, and found none. The lithium depletion occurs around 100–200 Myr for stars in the mass range of 0.06–0.08 M_{\odot} (Burke et al. 2004), thus giving a lower limit for the age of these 95 stars. This rules out *Gaia* DR2 2755265775727402112, as BANYAN Σ gives 97% Columba membership probability, while the age of the association is only 42 Myr (Bell et al. 2015), thus the star should still show lithium absorption.

To summarise, we have age estimates from the following sources (prioritizing them in the following order, removing intersections): 12 from moving group membership, 5 from comoving pairs and 71 from kinematics. These are tabulated in Table 2, and their distribution is plotted in Fig. 15. The number of stars in our sample with different estimated parameters are shown in Fig. 16.

4. Results and discussion

4.1. Notes on individual stars

The most flaring stars of the sample are *Gaia* DR2 1295931997030930432 (5 flares), 3200303384927512960 (10 flares) and 4989399774745144448 (5 flares). Figure 17 shows the available *TESS* light curves. Taking into account their different apparent magnitudes, these stars show a flaring rate comparable to TRAPPIST-1, as the downgraded K2 light curve from Sect. 3.3.1 yielded 8 flare events in 70^d of observation. While there is no trace in the literature of *Gaia* DR2 1295931997030930432, we know a bit more about the other two stars. *Gaia* DR2 3200303384927512960 (= 2MASS J04402325-0530082) appears in the sample of surveying nearby M-dwarfs

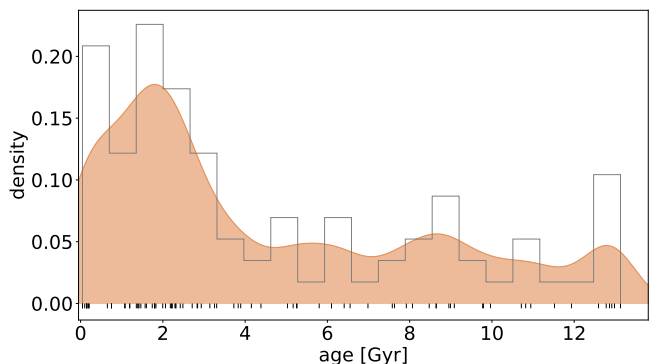


Fig. 15. The distribution of the ages of the stars in the sample. The kernel density estimation is calculated with Gaussian kernel with 0.6 Gyr bandwidth. Ticks below the curve show the individual data points.

searching for brown dwarfs in Nguyen-Thanh et al. (2020) where a SED fit is presented with $T_{\text{eff}} = 2600$ K and $\log g = 4.5$. *Gaia* DR2 4989399774745144448 (= 2MASS J01025100-3737438) is listed as flaring star by Mondrik et al. (2019) using observations from the M_{Earth} photometric survey. Finally, we note that the well-known and observed flare star *Gaia* DR2 4339417394313320192 = vB8 (2MASS J16553529-0823401), which has a measured magnetic field (2.8 ± 0.4 kG, Shulyak et al. 2019), is also included in our sample, but was not observed by *TESS* yet.

4.2. Periods

Photometric observations of TRAPPIST-1 yielded different values for its rotational period: 0.819^d from Spitzer infrared data (Roettenbacher & Kane 2017), 1.60^d from TRAPPIST-South (Gillon et al. 2016), 3.30^d from K2 (Luger et al. 2017; Vida et al. 2017). The reason for the discrepancy could be the changing pattern of spots on the surface that could imitate e.g. half or one-fourth of the real period. Such effect of quickly evolving spot pattern was not observed in our sample, mainly due to the relatively short observing time. Out of the 42 stars with periodic signal, *Gaia* DR2 1656001233124961152 was observed for the longest time (11 sectors). To find potential evidence of changing spot pattern, we compared the Lomb-Scargle periodograms of each sector, and employed Short Term Fourier Transform (see e.g., Kolláth & Oláh 2009). While the main period was only detected in 7 out of the 11 sectors, it is unclear whether it stems from some change in spot configuration, or just data systematics and noise. The half of this period was not detected in any of the sectors.

The histogram of the detected periods of TRAPPIST-1 analogues is plotted in Fig. 8. The distribution seems to be unimodal and follow a log-normal distribution. We performed a Shapiro-Wilk test (Shapiro & Wilk 1965) on the logarithm of the periods, and it could not reject the null hypothesis of normal distribution ($p = 0.37$). As a test for unimodality, we fitted the $\log P_{\text{rot}}$ dataset with a mixture of N Gaussians. The $N = 1$ model was clearly preferred by the Bayesian Information Criterion (with $\mu = 0.6^d$ mean and $\sigma = 0.6^d$ scatter). To put this into context, we compare it with other distributions from the literature. We try to separate each distribution using Gaussian Mixture models with the number of components determined from the Bayesian Information Criterion. We note that we use the logarithm of the periods, but transform the values back to make comparison easier.

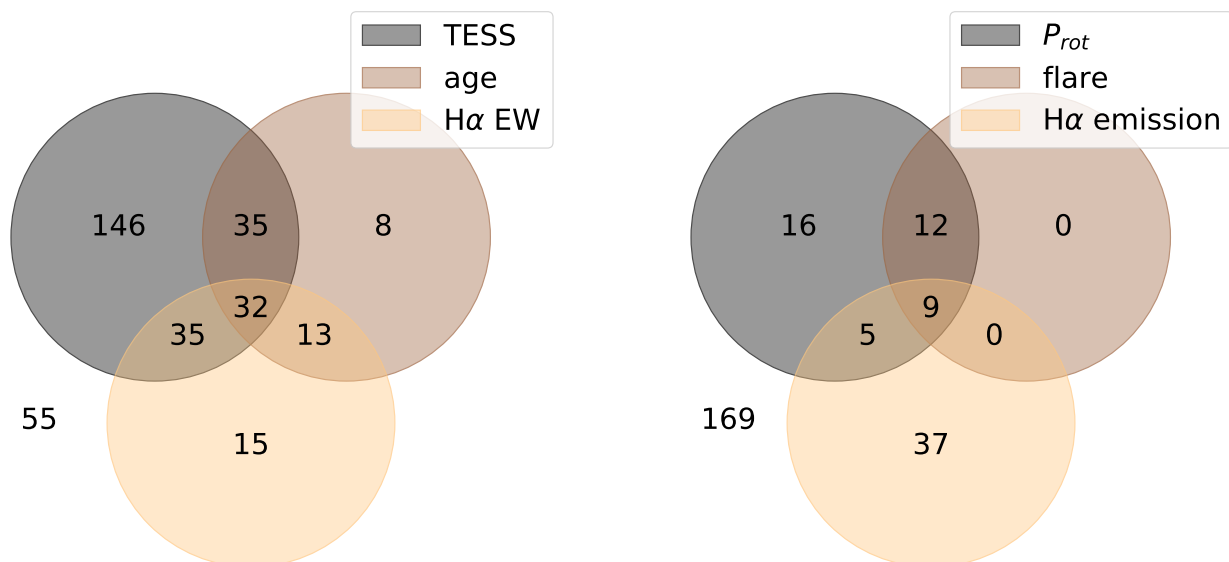


Fig. 16. Venn diagrams with the main properties of our sample. *Left:* The number of stars with available *TESS* light curve, age estimate and calculated H α EW from the whole sample of 339 stars. *Right:* The number of stars with detected period, flaring and H α emission (where the EW is at least 1σ above zero), only for the 248 stars with available *TESS* observation.

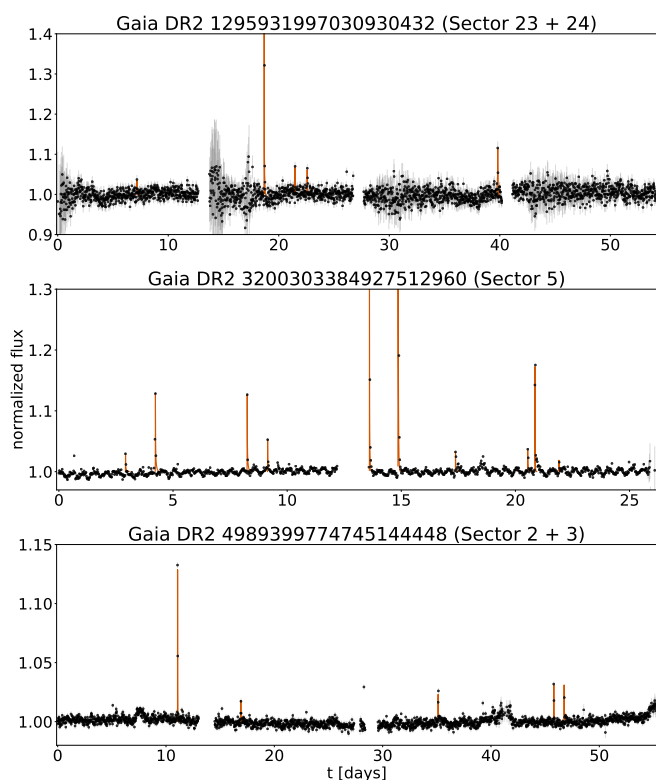


Fig. 17. The three most flaring targets from the sample, with $G_{RP} = 15.^m8$, $13.^m4$ and $13.^m8$, respectively. The detected flares are marked with orange.

The period distribution of early-to-mid M-dwarfs in the *Kepler* field was drawn first by McQuillan et al. (2013) based on 10 months of data. While they found a distinct group of

shorter period stars making up $\sim 8\%$ of the full sample, the most striking feature is the emergence of bimodality for longer periods, possibly arising from two distinct waves of star formation. The best Gaussian Mixture fit is achieved with the following 3 components: $(\mu_1, \sigma_1) = (3^d, 3^d)$ for the fast rotators, and $(\mu_2, \sigma_2) = (18^d, 4^d)$, $(\mu_3, \sigma_3) = (34^d, 7^d)$ for the longer periods. Later, Rappaport et al. (2014) using all 16 quarters of *Kepler* data detailed the period distribution of 297 M-dwarfs in the short period range. A two component fit to their data yields $(\mu_1, \sigma_1) = (0.4^d, 0.2^d)$, $(\mu_2, \sigma_2) = (1.2^d, 0.4^d)$. Using ground-based photometry from the MEarth Project, Newton et al. (2016, 2018) compiled the rotational period of ~ 600 mid-to-late M-dwarfs, also finding bimodality in the distribution. Fitting a Gaussian Mixture model to the logarithm of Grade A and B rotational periods from Newton et al. (2016, 2018) gives the following parameters: $(\mu_1, \sigma_1) = (0.6^d, 0.5^d)$ for the fast rotators, $(\mu_2, \sigma_2) = (93^d, 25^d)$ for the slow rotators, and a wide (possibly background) component in between: $(\mu_3, \sigma_3) = (6^d, 9^d)$.

These support that the cutoff in Fig. 8 is not entirely due to the 5^d upper limit in our period detection method, but there really is a dearth of objects with periods above a few days. Also the distribution seems to be consistent with the MEarth dataset, even with the truncation. It is likely that many stars from our sample belong to the slow rotating group ($P_{rot} \sim 100^d$), making one or two sectors of *TESS* data insufficient to reliably measure their periods.

Figure 18 shows really weak correlation between $\log P_{rot}$ and age, if any (0.43 Pearson correlation coefficient, with $p = 0.09$). There are several ways how P_{rot} can evolve (see Bouvier et al. 2014 for an overview), one of which is the initial spin up due to contraction. However, the stars in our sample are likely older than the typical spin up timescale, as illustrated in Fig. 20. After reaching the main sequence, UCDS evolve slowly, losing angular momentum with stellar wind. While this mechanism is effective for solar-type stars, UCDS spin down slowly, retaining their fast

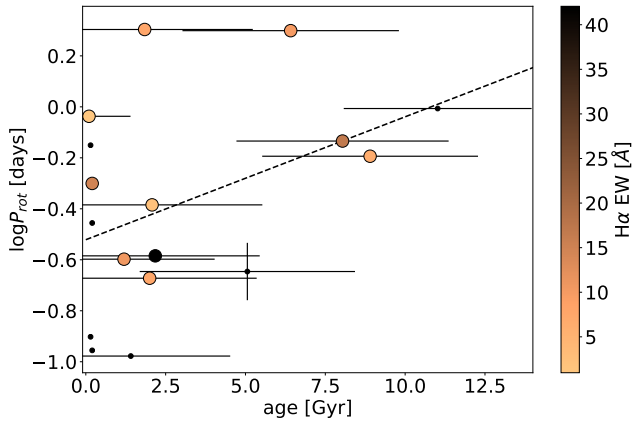


Fig. 18. Age and rotational periods for the sample. Dashes line shows a linear fit, small black points show stars without H α EW measurement.

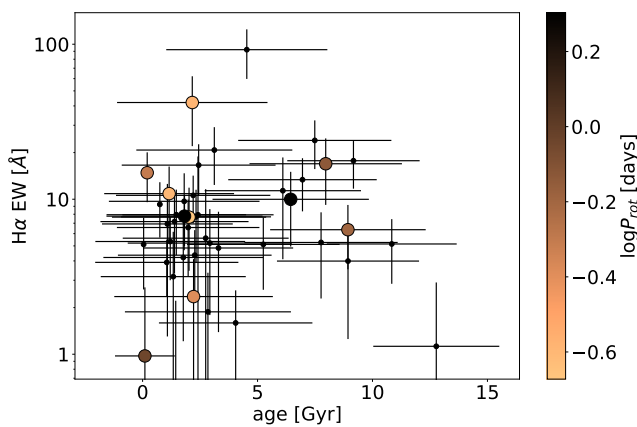


Fig. 19. Age and H α emission. There appears to be no clear trend with the rotational period.

rotation for Gyr timescales (see e.g., Reiners & Mohanty 2012; Newton et al. 2016). Irwin et al. (2011) studied a sample of 41 fully convective field M-dwarfs with P_{rot} measured from MEarth data. In their Fig. 13, they show age vs P_{rot} for their sample and also for several open clusters. Viewing only stars older than ~ 10 Myr and with $P_{\text{rot}} > 10^4$ gives a similarly large scatter as Fig. 18 here.

According to Fig. 19, the H α emission does not seem to correlate with age or P_{rot} . A possible explanation could be the saturated activity in these late type stars. Roettenbacher & Kane (2017) showed that the Rossby number $R_0 = P_{\text{rot}}/\tau_c$ is below 0.1 for TRAPPIST-1, and in fact for all stars with measured P_{rot} in our sample, taking $\tau_c = 70^{\text{d}}$ for the convective turnover time (following Reiners & Basri 2010). This means that the rotation rate no longer influences the activity of the 42 fast rotators found here. It can be seen in Fig. 16 that one-fourth of the stars with detected H α emission are fast rotators.

4.2.1. Flare frequency distribution

With the estimated flare energies from Sect. 3.3, the cumulative number of flares above given energies – the flare frequency distribution (FFD) – is shown in Fig. 21. It includes flares from 21 stars, all of which have measured rotational periods (see Fig. 16). We note that normally the FFD is plotted only for a single star,

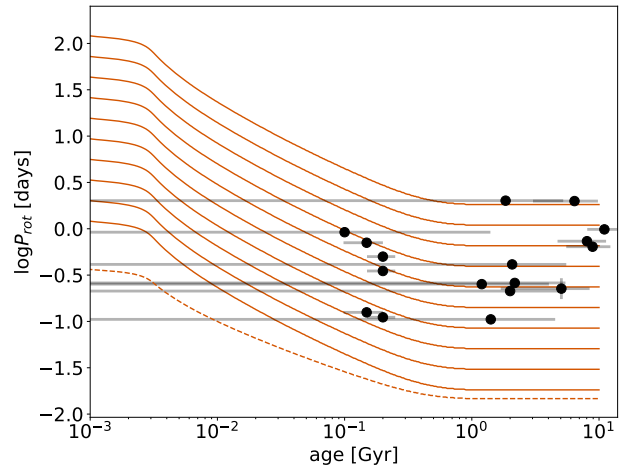


Fig. 20. Rotational period vs age for the TRAPPIST-1 analogues, compared with $M = 0.09 M_{\odot}$ evolutionary tracks from Baraffe et al. (2015), assuming angular momentum conservation with different initial P_{rot} values. The dashed line shows the breakup period $P_{\text{crit}}[\text{days}] = 0.116(R/R_{\odot})^{3/2}(M/M_{\odot})^{-1/2}$ from Herbst et al. (2001).

but here we used the whole sample, since most flaring stars showed only one event. This way, the composite FFD can be treated as an "average" FFD of the whole sample, including stars with different parameters, most notably different ages. However, according to Fig. 18 and Fig. 19 the ages of the stars do not really affect their activity levels, i.e., no clear trend is found between the age and the rotational periods and/or H α emission. The original FFD was corrected by dividing with the averaged completeness curve shown in Fig. 13. The corrected FFD was fitted with a linear function on log–log scale, yielding

$$\log(\nu[\text{day}^{-1}]) = (-1.11 \pm 0.02) \log(E_{\text{TESS}}[\text{erg}]) + (33.4 \pm 0.8) \quad (8)$$

where ν is the cumulative flare rate. This results in $\alpha = 2.11 \pm 0.02$ power law index, where

$$\frac{dN(E_{\text{TESS}})}{dE_{\text{TESS}}} \propto E_{\text{TESS}}^{-\alpha} \quad (9)$$

As the uncertainty due to the completeness correction was taken into account in the fit, the lower energy part had only negligible contribution. Fitting only above the break point at $\log E_{\text{TESS}} = 32$ gives $\alpha = 2.11 \pm 0.05$.

Vida et al. (2017) created the FFD of TRAPPIST-1 using short cadence *Kepler* K2 data. To compare the flare energies between *Kepler* and *TESS*, we calculated an approximate conversion factor by assuming (9000 ± 500) K black body spectrum for the emitting region (Kretzschmar 2011). We then convolved the spectral response functions of the instruments with the black body spectrum, and integrated over wavelength. Thus, the flare energies from *Kepler* can be converted to flare energies in the *TESS* bandpass as follows:

$$E_{\text{TESS}} = (0.72 \pm 0.02)E_{\text{Kepler}}, \quad (10)$$

This results in a 0.14 shift on logarithmic energy scale. Similarly, an approximate conversion factor to bolometric flare energy was calculated using a (9000 ± 500) K black body:

$$E_{\text{bol}} = (6.0 \pm 0.5)E_{\text{TESS}} \quad (11)$$

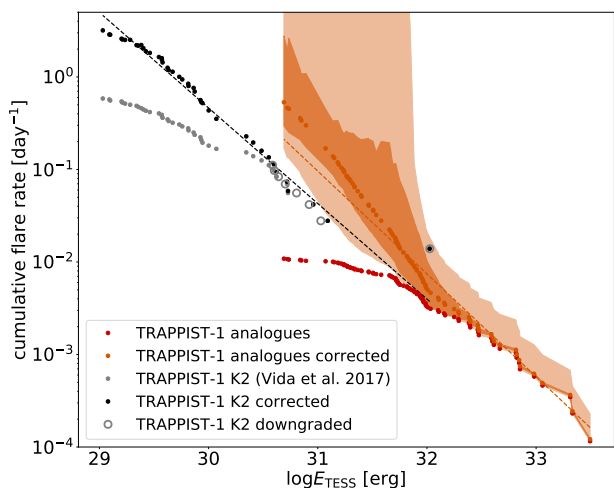


Fig. 21. Composite flare frequency distribution for the whole sample. Red points are the original values, orange points are corrected for flare recovery rate (orange line in Fig 13), and shaded regions are the 1 and 2 σ confidence intervals. The FFD of TRAPPIST–1 with K2 short cadence data from Vida et al. (2017) is also plotted for reference, converted to the *TESS* bandpass, and also its correction for completeness. Grey circles shows the flares recovered from the K2 light curve of TRAPPIST–1 downgraded to imitate a hypothetical *TESS* observation (with added noise, and re-sampled to 30-min cadence). Dashed lines show linear fits.

We note that while the *Kepler*–*TESS* conversion was relatively insensitive to the assumed black body temperature, it is not the case for the bolometric conversion. While $T = 9000$ K is generally used in the literature for the effective flare temperature (see e.g. Osten & Wolk 2015), Howard et al. (2020) demonstrated that superflares can emit at significantly higher temperatures. So the bolometric flare energies should be treated with caution, as they are likely lower limits. Before applying Equation 10, the K2 flare energies were recalculated using $L_{\text{Kepler}} = 5.6 \times 10^{28} \text{ erg s}^{-1}$ from Sect. 3.3, since Vida et al. (2017) used a different luminosity. Figure 21 also shows the K2 FFD and its downgraded version from Sect. 3.3.1. It can be seen that the measurements presented here are complementary to TRAPPIST–1, as they probe a higher energy range not observed before. The K2 FFD was also fitted with a line on log–log scale, taking into account the completeness correction from Sect. 3.3.2, and omitting the highest energy point which seems to deviate from the trend, resulting in:

$$\log(\nu[\text{day}^{-1}]) = (-1.03 \pm 0.02) \log(E_{\text{TESS}}[\text{erg}]) + (30.7 \pm 0.6) \quad (12)$$

This yields $\alpha = 2.03 \pm 0.02$ for TRAPPIST–1, a value consistent with the one found for our sample, suggesting that the FFD can be described by a single power law. Not using the correction for recovery rate would give $\alpha = 1.59 \pm 0.02$, a significantly shallower slope.

Hawley et al. (2014) analysed the flare rate of early-to-mid M-dwarfs with *Kepler* short cadence data, and found the steepest power law index $\alpha = 2.32$ on the latest M-dwarf binary in their sample, GJ 1245 AB (M5+M5). Once the light curve of the binary was separated by Lurie et al. (2015), the two independent power law indices changed to $\alpha = 1.99 \pm 0.02$ and $\alpha = 2.03 \pm 0.02$. Paudel et al. (2018) used K2 light curves to study flares on 10 UCDs (including TRAPPIST–1), and found α ranging from 1.34 to 2.04, with 1.66 mean. Gizis et al. (2017) used K2 data to study 3 young UCDs, and found $\alpha = 1.8$. For the mid-to-late M-dwarf sample of Medina et al. (2020), the power

law index is $\alpha = 1.98 \pm 0.02$. Yang & Liu (2019) compiled a catalogue of flares using all available long cadence *Kepler* light curves from DR25, and found an average $\alpha \approx 2$ power law index for all spectral types excluding A-stars, and also a $\sim 10\%$ incidence rate of flare stars among M-dwarfs, consistent with our result ($\sim 8\%$). So it appears that the slope found for the TRAPPIST–1 analogues here ($\alpha = 2.11$) is typical for late M-dwarfs, and consistent with TRAPPIST–1 itself ($\alpha = 2.03$). It also confirms that the same power law index is further applicable for one or two orders of magnitude larger flares. According to Aschwanden et al. (2016), magnetic and thermal energies dominate around $\alpha \approx 2.0$, opposed to nonthermal energy around $\alpha \approx 1.4$.

4.3. Habitability

Out of a sample of 57 exoplanets studied by Jagadeesh et al. (2018), TRAPPIST–1f is the closest to Earth in terms of Earth Similarity Index, Active and Cryptobiotic Tardigrade Index, meaning that life – as we know it – may survive on its surface (especially extremophile organisms like *tardigrades*). And while *Kepler* searched for exoplanets around solar-like stars, the number of detections around M-dwarfs is expected to grow with *TESS*. So the question of habitability around UCDs – especially TRAPPIST–1 – is timely.

Late-type dwarfs are important for exoplanet habitability studies since they spend billions of years on the main sequence, giving life enough time to emerge on the surface of planets orbiting them. However, the magnetic activity of these stars can endanger the habitability of the orbiting planets. One of the hazards is the erosion of the planetary atmosphere through intense electromagnetic and particle radiation. To preserve their atmospheres, the planets need a strong magnetic field, even 10–1000 times stronger than Earth’s magnetosphere (Vidotto et al. 2013). We know from the Sun that a large portion of flares are accompanied by CMEs, that are especially harmful if they reach the planetary atmosphere. Apart from the magnetosphere of the planets, Mullan et al. (2018) argue that the host star itself can trap the CMEs if it has sufficient magnetic field. They calculate a global 1.4–1.75 kG dipole field for TRAPPIST–1, which is strong enough to suppress even $10^{34} - 10^{35}$ erg events (assuming that flares are accompanied by CMEs with comparable energy). Furthermore, successful CMEs seem to be very rare in late-type dwarfs empirically, 90–98% of the eruptions do not reach the escape velocity, suggesting that electromagnetic radiation would be a larger factor for atmosphere erosion than particles (Vida et al. 2016, 2019a). This suggests that the planets of TRAPPIST–1 are safe CME-wise assuming the FFD from Fig. 21. And even if energetic flares/CMEs would erode the atmosphere of young planets and deplete their water reservoir in the early stages of their evolution, the replenishment of the ocean is possible through asteroid bombardment events (Dencs & Regály 2019). In this scenario, late M-dwarfs are not likely to erode their secondary atmospheres, after their primordial H/He envelope is gone (Atri & Mogan 2021). Dong et al. (2018) reached a similar conclusion for TRAPPIST–1, showing that the outer planets can retain their atmospheres for billions of years.

Once an atmosphere or even an ocean is present, abiogenesis is possible. The other hazardous effect of magnetic activity is the increased UV radiation during stellar flares that could harm simple or more evolved organisms (we note however that the UV radiation of flares might be the source that powers prebiotic photochemistry, see e.g. Ranjan et al. 2017). Estrela et al.

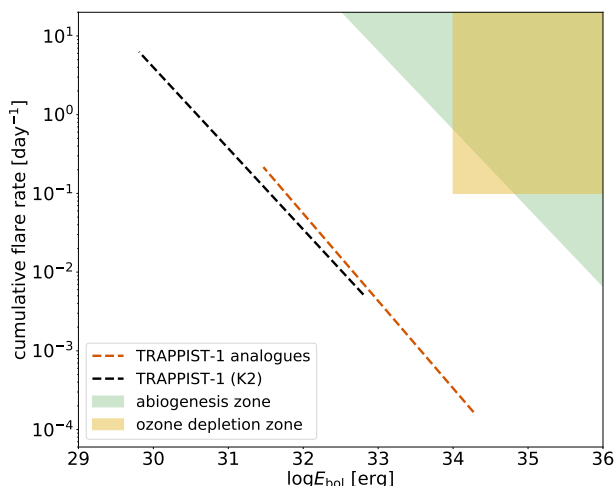


Fig. 22. Flare frequency distribution showing the region where abiogenesis is possible (Rimmer et al. 2018), and where ozone depletion can occur (Tilley et al. 2019). Dashed lines are the linear fits from Fig. 21. We note the use of E_{bol} instead of E_{TESS} .

(2020) studied the impact of superflares on two different bacteria (*E. coli* and *D. radiodurans*) on the TRAPPIST-1 planets. They found that an ozone layer or a few meters deep ocean is sufficient for the bacteria to survive the largest flares observed by *Kepler* K2. Abrevaya et al. (2020) showed that ozone is not the only option for a protective atmosphere, and a combination of CO_2 and N_2 could also suffice.

The FFD presented here includes flares with higher energies than ever observed on TRAPPIST-1 before, and it seems that the FFD can still be described by a single power law with $\alpha \approx 2$. Figure 22 shows the schematic FFD along with regions where ozone depletion and abiogenesis can be expected. Tilley et al. (2019) estimated that the ozone layer of unmagnetized planets can be fully destroyed if the rate of $E_{\text{bol}} > 10^{34}$ erg superflares reaches 0.1 day^{-1} . According to Rimmer et al. (2018), the lower limit on the FFD where abiogenesis is possible is also a power law, with -1 exponent. Their original relation used U-band energy, but we adopt the formula of Glazier et al. (2020) with E_{bol} (using blackbody conversion factors from Osten & Wolk 2015), thus giving:

$$\nu(E_{\text{bol}}) > 6.6 \times 10^{33} \times E_{\text{bol}}^{-1} \quad (13)$$

And since $\alpha \approx 2$ corresponds to $1 - \alpha \approx -1$ exponent, the border of the abiogenesis zone is approximately parallel to the FFD of TRAPPIST-1, hinting that they do not intersect, not even at higher energies. These strengthen the findings of Glazier et al. (2020), that the current flare rate of TRAPPIST-1 is unlikely to cause ozone depletion or initiate abiogenesis.

5. Summary and conclusions

We analysed 248 TRAPPIST-1 analogues using 30-min *TESS* light curves, we can summarise our findings as follows:

1. We found altogether 94 flare events on 21 stars. From the targets, in 42 a periodic light curve modulation was found (likely due to rotation) in the range of $0.1\text{--}5^{\text{d}}$ (we searched only for periods up to 5^{d}). All the 21 stars with flares show rotational modulation as well.

2. We estimated the approximate age of 88 stars from the sample with various methods, but did not find a convincing correlation between age, rotation rate and $H\alpha$ emission.
3. The power law slope of the composite FFD was found to be similar to the value for TRAPPIST-1, hinting that it is not an especially active/inactive star for its spectral type. Combining the light curves of objects in the sample enabled us to find stronger flares than ever observed on TRAPPIST-1 before, suggesting that they actually occur, even if rarely. We found that flares with $E_{\text{TESS}} > 10^{33}$ erg ($E_{\text{bol}} \gtrsim 10^{34}$ erg) can be expected every few decades.
4. It seems that the flaring rate of TRAPPIST-1 is not sufficient to fully destroy the possible ozone layer of its planets, nor to initiate abiogenesis via UV radiation. Glazier et al. (2020) reached a similar conclusion, using an upper limit for the superflare rate from Evryscope observations.

Acknowledgements. The authors would like to thank the anonymous referee for improving the quality of the paper with helpful comments and suggestions. BS was supported by the ÚNKP-19-3 New National Excellence Program of the Ministry for Innovation and Technology. KV was supported by the Bolyai János Research Scholarship of the Hungarian Academy of Sciences. This project has been supported by the Lendület Program of the Hungarian Academy of Sciences, project No. LP2018-7/2019, the NKFI KH-130526 and NKFI K-131508 grants, the Hungarian OTKA Grant No. 119993 and by the NKFI grant 2019-2.1.11-TÉT-2019-00056. On behalf of "Analysis of space-borne photometric data" project we thank for the usage of MTA Cloud (<https://cloud.mta.hu>) that helped us achieving the results published in this paper. Authors acknowledge the financial support of the Austrian-Hungarian Action Foundation (95 öu3, 98 öu5, 101 öu13). This paper includes data collected by the *TESS* mission. Funding for the *TESS* mission is provided by the NASA Explorer Program. This research has benefitted from the Ultracool RIZZO Spectral Library (<http://dx.doi.org/10.5281/zenodo.11313>), maintained by Jonathan Gagné and Kelle Cruz.

References

- Abrevaya, X. C., Leitzinger, M., Opezzo, O. J., et al. 2020, *MNRAS*, 494, L69
- Almeida-Fernandes, F. & Rocha-Pinto, H. J. 2018, *MNRAS*, 476, 184
- Alvarado-Gómez, J. D., Drake, J. J., Cohen, O., Moschou, S. P., & Garraffo, C. 2018, *ApJ*, 862, 93
- Anglada-Escudé, G., Amado, P. J., Barnes, J., et al. 2016, *Nature*, 536, 437
- Angus, R., Morton, T. D., Foreman-Mackey, D., et al. 2019, *AJ*, 158, 173
- Aschwanden, M. J., Holman, G., O'Flanagan, A., et al. 2016, *ApJ*, 832, 27
- Atri, D. & Mogan, S. R. C. 2021, *MNRAS*, 500, L1
- Baraffe, I., Homeier, D., Allard, F., & Chabrier, G. 2015, *A&A*, 577, A42
- Bardalez Gagliuffi, D. C., Burgasser, A. J., Schmidt, S. J., et al. 2019, *ApJ*, 883, 205
- Baron, F., Lafrenière, D., Artigau, É., et al. 2019, *AJ*, 158, 187
- Bell, C. P. M., Mamajek, E. E., & Naylor, T. 2015, *MNRAS*, 454, 593
- Bouvier, J., Matt, S. P., Mohanty, S., et al. 2014, in *Protostars and Planets VI*, ed. H. Beuther, R. S. Klessen, C. P. Dullemond, & T. Henning, 433
- Burgasser, A. J., Logsdon, S. E., Gagné, J., et al. 2015, *ApJS*, 220, 18
- Burgasser, A. J. & Mamajek, E. E. 2017, *ApJ*, 845, 110
- Burke, C. J., Pinsonneault, M. H., & Sills, A. 2004, *ApJ*, 604, 272
- Cleveland, W. S. 1979, *Journal of the American Statistical Association*, 74, 829
- Cruz, K. L., Reid, I. N., Kirkpatrick, J. D., et al. 2007, *AJ*, 133, 439
- Cruz, K. L., Reid, I. N., Liebert, J., Kirkpatrick, J. D., & Lowrance, P. J. 2003, *AJ*, 126, 2421
- Davenport, J. R. A. 2016, *ApJ*, 829, 23
- Davenport, J. R. A., Hawley, S. L., Hebb, L., et al. 2014, *ApJ*, 797, 122
- Dencs, Z. & Regály, Z. 2019, *MNRAS*, 487, 2191
- Dong, C., Jin, M., Lingam, M., et al. 2018, *Proceedings of the National Academy of Science*, 115, 260
- Estrela, R., Palit, S., & Valio, A. 2020, *Astrobiology*, 20, 1465
- Fonnesbeck, C., Patil, A., Huard, D., & Salvatier, J. 2015, *PyMC: Bayesian Stochastic Modelling in Python*
- Gagné, J., Lafrenière, D., Doyon, R., Malo, L., & Artigau, É. 2015, *ApJ*, 798, 73
- Gagné, J., Mamajek, E. E., Malo, L., et al. 2018, *ApJ*, 856, 23
- Gaia Collaboration, Brown, A. G. A., Vallenari, A., et al. 2018, *A&A*, 616, A1
- Gaia Collaboration, Smart, R. L., Sarro, L. M., et al. 2020, *arXiv e-prints*, arXiv:2012.02061
- Gershberg, R. E. 1972, *Ap&SS*, 19, 75
- Gillon, M., Jehin, E., Lederer, S. M., et al. 2016, *Nature*, 533, 221

- Gillon, M., Triaud, A. H. M. J., Demory, B.-O., et al. 2017, *Nature*, 542, 456
- Gizis, J. E., Paudel, R. R., Mullan, D., et al. 2017, *ApJ*, 845, 33
- Glazier, A. L., Howard, W. S., Corbett, H., et al. 2020, *ApJ*, 900, 27
- Goldman, B., Röser, S., Schilbach, E., et al. 2013, *A&A*, 559, A43
- Gonzales, E. C., Faherty, J. K., Gagné, J., et al. 2019, *ApJ*, 886, 131
- Günther, M. N., Zhan, Z., Seager, S., et al. 2020, *AJ*, 159, 60
- Hawley, S. L., Davenport, J. R. A., Kowalski, A. F., et al. 2014, *ApJ*, 797, 121
- Herbst, W., Bailer-Jones, C. A. L., & Mundt, R. 2001, *ApJ*, 554, L197
- Howard, W. S., Corbett, H., Law, N. M., et al. 2020, *ApJ*, 902, 115
- Irwin, J., Berta, Z. K., Burke, C. J., et al. 2011, *ApJ*, 727, 56
- Jagadeesh, M. K., Roszkowska, M., & Kaczmarek, Ł. 2018, *Life Sciences and Space Research*, 19, 13
- Jordí, C., Gebran, M., Carrasco, J. M., et al. 2010, *A&A*, 523, A48
- Kolláth, Z. & Oláh, K. 2009, *A&A*, 501, 695
- Kretzschmar, M. 2011, *A&A*, 530, A84
- Lomb, N. R. 1976, *Ap&SS*, 39, 447
- Luger, R., Sestovic, M., Kruse, E., et al. 2017, *Nature Astronomy*, 1, 0129
- Lurie, J. C., Davenport, J. R. A., Hawley, S. L., et al. 2015, *ApJ*, 800, 95
- McQuillan, A., Aigrain, S., & Mazeh, T. 2013, *MNRAS*, 432, 1203
- Medina, A. A., Winters, J. G., Irwin, J. M., & Charbonneau, D. 2020, *ApJ*, 905, 107
- Mondrik, N., Newton, E., Charbonneau, D., & Irwin, J. 2019, *ApJ*, 870, 10
- Mullan, D. J., MacDonald, J., Dieterich, S., & Fauser, H. 2018, *ApJ*, 869, 149
- Namekata, K., Sakaue, T., Watanabe, K., et al. 2017, *ApJ*, 851, 91
- Newton, E. R., Irwin, J., Charbonneau, D., et al. 2016, *ApJ*, 821, 93
- Newton, E. R., Mondrik, N., Irwin, J., Winters, J. G., & Charbonneau, D. 2018, *AJ*, 156, 217
- Nguyen-Thanh, D., Phan-Bao, N., Murphy, S. J., & Bessell, M. S. 2020, *A&A*, 634, A128
- Osten, R. A. & Wolk, S. J. 2015, *ApJ*, 809, 79
- Pál, A. 2012, *MNRAS*, 421, 1825
- Paudel, R. R., Gizis, J. E., Mullan, D. J., et al. 2018, *ApJ*, 858, 55
- Petralia, A. & Micela, G. 2020, *Experimental Astronomy*, 49, 97
- Raetz, S., Stelzer, B., Damasso, M., & Scholz, A. 2020, *A&A*, 637, A22
- Ranjan, S., Wordsworth, R., & Sasselov, D. D. 2017, *ApJ*, 843, 110
- Rappaport, S., Swift, J., Levine, A., et al. 2014, *ApJ*, 788, 114
- Reid, I. N., Cruz, K. L., Kirkpatrick, J. D., et al. 2008, *AJ*, 136, 1290
- Reiners, A. & Basri, G. 2010, *ApJ*, 710, 924
- Reiners, A. & Mohanty, S. 2012, *ApJ*, 746, 43
- Reylé, C. 2018, *A&A*, 619, L8
- Ricker, G. R., Winn, J. N., Vanderspek, R., et al. 2015, *Journal of Astronomical Telescopes, Instruments, and Systems*, 1, 014003
- Rimmer, P. B., Xu, J., Thompson, S. J., et al. 2018, *Science Advances*, 4, eaar3302
- Roettenbacher, R. M. & Kane, S. R. 2017, *ApJ*, 851, 77
- Scargle, J. D. 1982, *ApJ*, 263, 835
- Shapiro, S. S. & Wilk, M. B. 1965, *Biometrika*, 52, 591
- Shulyak, D., Reiners, A., Nagel, E., et al. 2019, *A&A*, 626, A86
- Smart, R. L., Marocco, F., Sarro, L. M., et al. 2019, *MNRAS*, 485, 4423
- Stassun, K. G., Oelkers, R. J., Paegert, M., et al. 2019, *AJ*, 158, 138
- Tenenbaum, P. & Jenkins, J. M. 2018, *TESS Science Data Products Description Document*, EXP-TESSARC-ICD-0014 Rev D., (Baltimore, MD: STScI) <https://archive.stsci.edu/missions/tess/doc/EXP-TESS-ARC-ICD-TM-0014.pdf>
- Tilley, M. A., Segura, A., Meadows, V., Hawley, S., & Davenport, J. 2019, *Astrobiology*, 19, 64
- Van Doorselaere, T., Shariati, H., & Debosscher, J. 2017, *ApJS*, 232, 26
- Vida, K., Kóvári, Zs., Pál, A., Oláh, K., & Kriskovics, L. 2017, *ApJ*, 841, 124
- Vida, K., Kriskovics, L., Oláh, K., et al. 2016, *A&A*, 590, A11
- Vida, K., Leitzinger, M., Kriskovics, L., et al. 2019a, *A&A*, 623, A49
- Vida, K., Oláh, K., Kóvári, Zs., et al. 2019b, *ApJ*, 884, 160
- Vidotto, A. A., Jardine, M., Morin, J., et al. 2013, *A&A*, 557, A67
- Yang, H. & Liu, J. 2019, *ApJS*, 241, 29
- Zechmeister, M., Dreizler, S., Ribas, I., et al. 2019, *A&A*, 627, A49
- Zhan, Z., Günther, M. N., Rappaport, S., et al. 2019, *ApJ*, 876, 127

Table A.1. Rotational periods from the Lomb–Scargle analysis

Gaia DR2 source ID	period [days]	FAP	amplitude [mmag]	scatter [mmag]	#flares
1040681747033185152	0.23882 ± 0.00004	3.5e-73	9.1	11.5	2
1254110521784729984	0.26027 ± 0.00009	3.3e-78	21.1	32.0	0
1282632682337912832	0.37110 ± 0.00014	8.9e-41	4.2	7.4	1
1295931997030930432	0.25256 ± 0.00011	6.4e-22	6.3	15.5	5
1303076623589331968	3.53028 ± 0.04614	1.7e-04	4.7	25.4	0
1412377317863375488	0.91820 ± 0.00370	1.2e-05	10.3	78.1	0
1437716460972795392	4.88480 ± 0.09917	2.9e-04	1.8	36.0	0
1454104436971779328	0.64009 ± 0.00092	2.4e-14	3.6	12.1	1
1618010323247026560	0.41250 ± 0.00030	2.2e-22	0.9	3.8	1
1656001233124961152	0.81474 ± 0.04714	9.6e-05	4.8	25.3	3
1821315795663331456	0.22591 ± 0.05854	2.0e-08	3.6	18.3	1
1916411143300424832	0.82768 ± 0.00189	1.4e-08	9.4	28.2	0
1998109946788787456	0.95529 ± 0.00179	1.9e-17	9.4	35.3	0
2088442248714858368	1.45381 ± 0.24790	9.4e-11	9.4	39.7	0
2137903951084527488	0.39450 ± 0.00013	2.6e-58	10.7	15.3	3
2177877452238559104	0.35025 ± 0.00022	4.8e-19	2.7	6.6	0
229155579195699456	0.98491 ± 0.00101	6.8e-95	3.7	4.7	0
2336406413104712320	0.30911 ± 0.00008	2.9e-57	9.5	13.2	3
2349207644734247808	2.13867 ± 0.00221	6.0e-161	20.9	13.6	1
2472387757755767168	0.40031 ± 0.00033	5.1e-08	3.7	13.6	0
2883680659313632896	1.92203 ± 0.00778	1.6e-08	6.8	23.4	1
3197623290976364544	4.91369 ± 0.02047	2.0e-57	12.4	19.9	0
3200303384927512960	0.50062 ± 0.00019	4.5e-124	3.8	3.3	10
3475115115014143616	0.22498 ± 0.00007	3.5e-53	33.2	42.6	0
3830128624846458752	0.21266 ± 0.00003	1.1e-208	16.9	10.0	3
4733265410022963456	0.20460 ± 0.00004	2.0e-51	28.8	81.4	1
4967628688601251200	0.40391 ± 0.00020	5.5e-46	4.2	7.0	1
4971892010576979840	0.70254 ± 0.00074	7.1e-26	2.1	3.7	0
4989399774745144448	1.99002 ± 0.00607	5.2e-13	0.9	2.8	5
5809399363316630912	0.11082 ± 0.00001	4.9e-44	5.9	9.7	0
5856405272135505024	0.12529 ± 0.00006	1.4e-19	7.0	17.9	0
5983189339421393152	2.95347 ± 0.01652	3.0e-16	18.2	54.1	0
599891555546067072	0.73416 ± 0.00053	4.8e-105	8.6	8.9	3
6135947032490329472	1.47841 ± 0.00148	1.5e-119	2.6	2.9	3
6224387727748521344	2.01107 ± 0.00247	1.7e-316	6.8	3.7	0
6525046188759705728	0.15211 ± 0.00008	8.4e-05	3.9	16.3	1
6783123184369906816	0.41521 ± 0.00011	2.2e-85	9.0	10.6	3
779689533779300736	0.10527 ± 0.00001	8.8e-92	12.2	14.9	0
847228998317017472	1.04848 ± 0.00137	6.6e-22	6.7	16.2	0
89186168428165632	0.70691 ± 0.00082	4.0e-48	12.3	17.1	0
901941452829250560	0.34495 ± 0.00016	2.4e-54	7.3	10.0	3
977653372545774336	1.03019 ± 0.00170	2.1e-34	15.7	30.1	0

Appendix A: Measured rotational periods

We present the rotational periods in Table A.1. If the period was measurable in multiple sectors, the average period is given (the differences between the period values of the same star are consistent with the nominal error bars). In such cases the FAP value is calculated as the geometric mean of individual FAPs. The phase-folded light curves are plotted in Fig. A.1.

Appendix B: Flare events

We present the parameters of all 94 individual flare events in Table B.1. In some cases the MCMC fit did not converge, for those events $t_{1/2,fit}$, A_{fit} and ED_{fit} are omitted, and $t_{peak,fit}$ only indicates the time of the highest flux value.

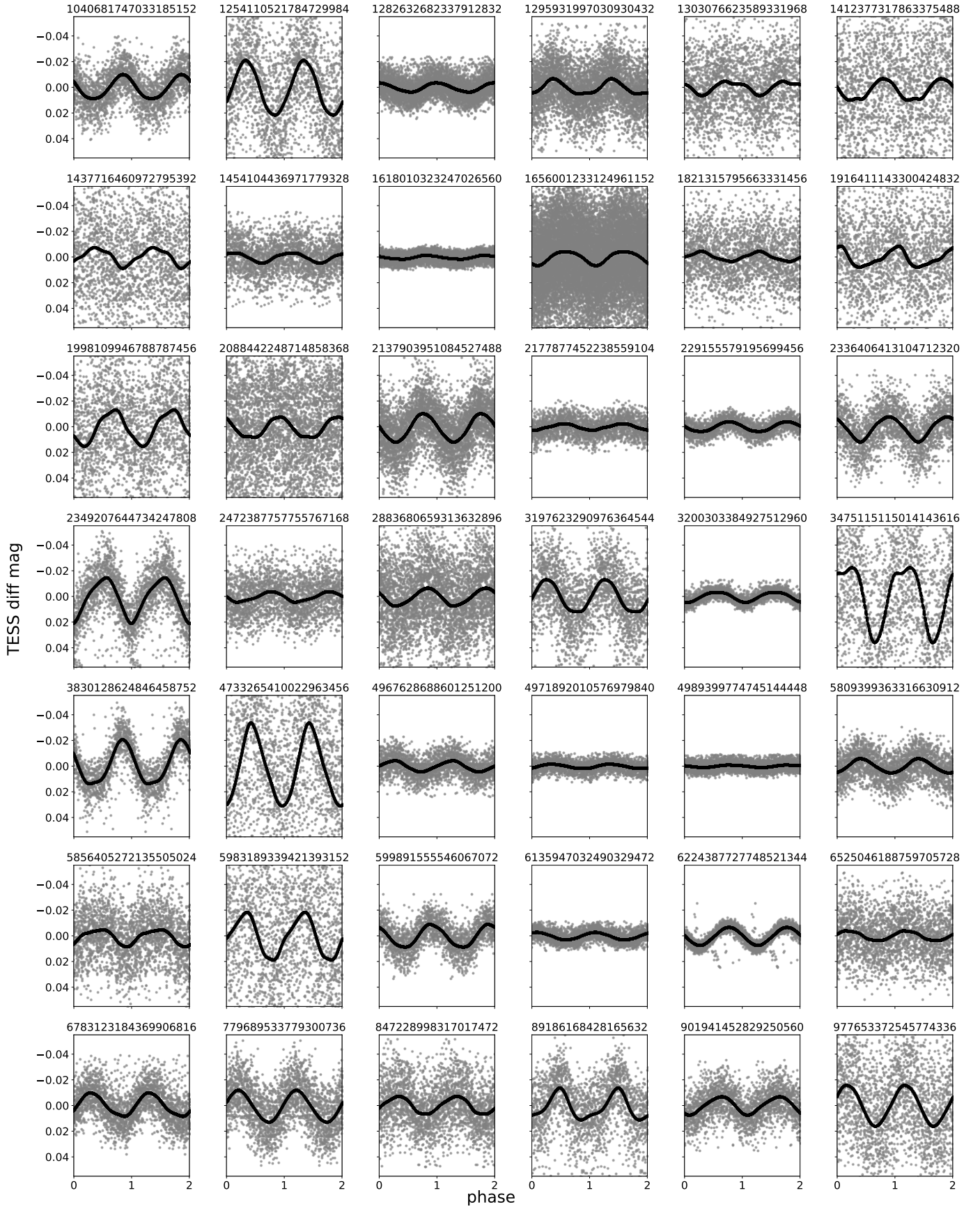


Fig. A.1. Light curves of stars with detected periodicity, folded with the average period from Table A.1. Black line denotes the smoothed light curve.

Table B.1. Flare parameters. The fitted values are removed where the MCMC fit did not converge. The column E_{sum} equals to ED_{sum} multiplied by the luminosity of TRAPPIST-1 in the *TESS* bandpass.

Gaia DR2 source ID	$t_{\text{peak,fit}}$ [JD-2 450 000]	$t_{1/2,\text{fit}}$ [min]	A_{fit}	ED_{fit} [min]	ED_{sum} [min]	E_{sum} [10^{31} erg]
1040681747033185152	8856.732 ± 0.010	8.3 ± 6.3	0.28 ± 0.31	4.4 ± 3.6	3.6 ± 1.5	4.5 ± 1.9
1040681747033185152	8864.857 ± 0.007	9.9 ± 14.5	0.12 ± 0.16	2.8 ± 1.6	1.6 ± 1.2	2.0 ± 1.5
1078021436789455872	8891.802 ± 0.001	9.3 ± 0.7	1.67 ± 0.17	28.8 ± 1.8	55.6 ± 1.3	70.0 ± 1.6
1269789664970320512	8974.403	–	–	–	2.3 ± 2.4	2.9 ± 3.1
1282632682337912832	8972.577 ± 0.000	7.8 ± 0.5	2.98 ± 0.27	42.4 ± 1.3	23.7 ± 1.0	29.9 ± 1.2
1295931997030930432	8946.826 ± 0.000	7.3 ± 0.7	2.80 ± 0.36	37.7 ± 1.7	32.5 ± 1.2	41.0 ± 1.5
1295931997030930432	8935.294 ± 0.196	17.1 ± 34.8	0.05 ± 0.09	1.7 ± 1.3	1.7 ± 1.0	2.1 ± 1.3
1295931997030930432	8949.608 ± 0.006	7.3 ± 5.0	0.23 ± 0.23	3.3 ± 1.8	1.6 ± 1.0	2.0 ± 1.3
1295931997030930432	8950.715 ± 0.007	18.3 ± 11.4	0.12 ± 0.09	4.5 ± 1.2	3.9 ± 1.0	4.9 ± 1.3
1295931997030930432	8967.940 ± 0.007	11.3 ± 5.6	0.32 ± 0.21	7.0 ± 2.3	5.2 ± 1.3	6.5 ± 1.7
1324598017513898752	8979.130 ± 0.006	14.4 ± 8.0	0.28 ± 0.22	8.4 ± 2.7	6.8 ± 1.9	8.6 ± 2.4
13533892921879936	8421.808 ± 0.000	11.2 ± 0.8	1.88 ± 0.17	38.6 ± 1.4	23.2 ± 1.3	29.2 ± 1.7
13533892921879936	8426.255 ± 0.006	9.2 ± 5.2	0.26 ± 0.22	4.8 ± 2.2	4.3 ± 1.2	5.5 ± 1.5
1454104436971779328	8953.733 ± 0.007	12.7 ± 9.5	0.11 ± 0.11	3.0 ± 1.2	2.3 ± 0.9	2.9 ± 1.1
1516293918446402176	8932.112 ± 0.068	34.6 ± 114.1	0.10 ± 0.12	7.2 ± 4.4	5.6 ± 2.7	7.0 ± 3.4
1595520568815311744	8959.654 ± 0.004	86.4 ± 17.0	0.05 ± 0.01	7.6 ± 0.9	4.8 ± 0.5	6.1 ± 0.7
1618010323247026560	8742.805 ± 0.000	5.3 ± 1.1	0.32 ± 0.11	3.2 ± 0.5	1.3 ± 0.2	1.7 ± 0.2
1656001233124961152	8859.091 ± 0.005	11.8 ± 7.7	0.32 ± 0.22	7.8 ± 3.8	6.9 ± 3.1	8.6 ± 3.9
1656001233124961152	8905.739 ± 0.002	11.9 ± 2.0	1.74 ± 0.38	38.2 ± 5.0	51.9 ± 2.9	65.4 ± 3.7
1656001233124961152	8971.909 ± 0.003	30.4 ± 10.9	0.42 ± 0.15	23.7 ± 3.5	19.8 ± 3.0	24.9 ± 3.8
1688578285187648128	8881.346 ± 0.000	6.2 ± 0.9	1.53 ± 0.33	17.5 ± 1.5	14.1 ± 0.8	17.8 ± 1.0
1688578285187648128	8887.909 ± 0.000	4.8 ± 0.4	3.67 ± 0.63	32.1 ± 2.7	10.1 ± 0.9	12.7 ± 1.1
1688578285187648128	8896.180 ± 0.000	4.5 ± 0.5	2.77 ± 0.63	23.0 ± 2.6	7.1 ± 0.9	8.9 ± 1.1
1821315795663331456	8684.947 ± 0.003	10.3 ± 2.6	1.48 ± 0.54	28.1 ± 5.8	36.9 ± 3.3	46.5 ± 4.1
1902388491693623680	8759.986 ± 0.007	24.6 ± 28.1	0.10 ± 0.11	5.3 ± 2.4	4.2 ± 1.9	5.3 ± 2.4
2137903951084527488	8683.944 ± 0.006	14.6 ± 12.4	0.17 ± 0.16	5.4 ± 2.5	4.0 ± 2.3	5.1 ± 2.9
2137903951084527488	8694.827 ± 0.000	11.0 ± 2.0	2.12 ± 0.45	42.9 ± 2.9	31.6 ± 2.6	39.8 ± 3.3
2137903951084527488	8699.179 ± 0.166	42.2 ± 81.7	0.08 ± 0.10	6.3 ± 4.7	6.1 ± 3.0	7.7 ± 3.8
2267517023167123712	8892.860 ± 0.007	22.4 ± 11.0	0.23 ± 0.14	10.5 ± 2.2	7.8 ± 1.4	9.9 ± 1.8
2331849006126794880	8373.005 ± 0.006	18.3 ± 10.2	0.04 ± 0.03	1.7 ± 0.5	1.5 ± 0.4	1.9 ± 0.5
2331849006126794880	8379.617 ± 0.008	8.5 ± 4.6	0.18 ± 0.13	2.8 ± 0.8	1.8 ± 0.4	2.3 ± 0.5
2336406413104712320	8361.626 ± 0.000	15.2 ± 0.2	12.04 ± 0.28	335.5 ± 3.6	170.8 ± 2.9	215.2 ± 3.6
2336406413104712320	8369.367 ± 0.000	33.7 ± 1.1	2.32 ± 0.05	143.1 ± 1.8	163.0 ± 2.5	205.3 ± 3.1
2336406413104712320	8373.175 ± 0.003	6.4 ± 2.1	0.48 ± 0.35	5.9 ± 2.7	7.7 ± 1.3	9.7 ± 1.6
2349207644734247808	8396.660 ± 0.000	6.9 ± 0.1	16.41 ± 0.43	206.1 ± 2.0	247.8 ± 2.8	312.2 ± 3.5
2523162448812944640	8404.447 ± 0.003	13.8 ± 4.0	0.76 ± 0.27	20.3 ± 4.6	23.5 ± 3.0	29.6 ± 3.8
2523162448812944640	8405.779 ± 0.086	34.9 ± 73.7	0.11 ± 0.12	7.5 ± 4.9	6.1 ± 3.1	7.6 ± 4.0
2883680659313632896	8482.405 ± 0.003	11.3 ± 4.3	0.57 ± 0.24	12.7 ± 4.2	15.4 ± 2.8	19.4 ± 3.5
3200303384927512960	8440.910	–	–	–	1.5 ± 0.2	1.8 ± 0.3
3200303384927512960	8442.219	–	–	–	6.4 ± 0.2	8.1 ± 0.3
3200303384927512960	8446.240	–	–	–	4.4 ± 0.2	5.6 ± 0.3
3200303384927512960	8447.136	–	–	–	2.0 ± 0.2	2.5 ± 0.2
3200303384927512960	8451.596 ± 0.000	6.6 ± 0.3	1.52 ± 0.09	18.4 ± 0.4	19.3 ± 0.1	24.3 ± 0.2
3200303384927512960	8452.846 ± 0.000	5.7 ± 0.0	10.57 ± 0.11	111.0 ± 0.5	90.8 ± 0.2	114.4 ± 0.2
3200303384927512960	8455.366	–	–	–	1.7 ± 0.2	2.2 ± 0.3
3200303384927512960	8458.530	–	–	–	1.7 ± 0.2	2.2 ± 0.3
3200303384927512960	8458.847 ± 0.000	4.9 ± 0.2	2.57 ± 0.18	23.0 ± 0.7	11.6 ± 0.2	14.7 ± 0.3
3200303384927512960	8459.897 ± 0.006	6.0 ± 3.8	0.09 ± 0.09	1.0 ± 0.5	0.4 ± 0.2	0.5 ± 0.3
3830128624846458752	8520.216 ± 0.004	6.8 ± 2.1	0.51 ± 0.42	6.6 ± 3.2	8.1 ± 0.9	10.2 ± 1.1
3830128624846458752	8521.045 ± 0.006	12.5 ± 7.5	0.20 ± 0.17	5.4 ± 2.2	3.7 ± 0.8	4.7 ± 1.1
3830128624846458752	8527.493 ± 0.000	10.0 ± 1.3	0.91 ± 0.14	16.6 ± 0.7	15.5 ± 0.6	19.6 ± 0.8
4694260956582093440	8360.236	–	–	–	5.3 ± 3.3	6.6 ± 4.2
4733265410022963456	8393.489 ± 0.001	12.1 ± 2.4	0.89 ± 0.15	20.6 ± 3.7	30.9 ± 2.9	38.9 ± 3.7
4742124385662135168	8360.320 ± 0.006	18.1 ± 9.8	0.26 ± 0.17	9.7 ± 2.9	7.7 ± 2.4	9.7 ± 3.1
4825880783419986432	8458.730 ± 0.006	8.8 ± 2.3	0.43 ± 0.20	6.9 ± 2.3	4.5 ± 0.7	5.7 ± 0.9
4866773609425146496	8442.740	–	–	–	2.0 ± 2.5	2.5 ± 3.1
4967628688601251200	8400.533 ± 0.008	19.0 ± 15.0	0.05 ± 0.05	2.0 ± 0.6	1.4 ± 0.6	1.7 ± 0.8
4989399774745144448	8365.200 ± 0.000	4.1 ± 0.6	1.14 ± 0.39	8.4 ± 1.5	5.8 ± 0.2	7.3 ± 0.3
4989399774745144448	8371.037 ± 0.002	11.3 ± 7.7	0.09 ± 0.06	1.8 ± 0.3	1.1 ± 0.3	1.4 ± 0.3
4989399774745144448	8389.263 ± 0.000	4.2 ± 1.1	0.45 ± 0.26	3.4 ± 1.0	1.2 ± 0.2	1.5 ± 0.3

Table B.1. Flare parameters. The fitted values are removed where the MCMC fit did not converge. The column E_{sum} equals to ED_{sum} multiplied by the luminosity of TRAPPIST-1 in the *TESS* bandpass (continued).

4989399774745144448	8399.930 ± 0.000	5.1 ± 1.6	0.23 ± 0.13	2.2 ± 0.5	1.5 ± 0.2	1.9 ± 0.3
4989399774745144448	8400.896 ± 0.006	4.4 ± 1.8	0.18 ± 0.14	1.4 ± 0.8	0.6 ± 0.2	0.7 ± 0.3
5055805741577757824	8414.170 ± 0.006	3.9 ± 2.3	0.21 ± 0.20	1.5 ± 1.1	0.9 ± 0.3	1.2 ± 0.4
5055805741577757824	8418.171 ± 0.229	12.2 ± 34.2	0.05 ± 0.12	0.9 ± 3.5	0.4 ± 0.3	0.5 ± 0.4
5055805741577757824	8429.918 ± 0.006	5.9 ± 4.9	0.09 ± 0.10	1.0 ± 0.6	0.4 ± 0.3	0.5 ± 0.3
5433620854830342272	8545.027 ± 0.006	15.4 ± 9.4	0.30 ± 0.22	9.6 ± 3.5	8.6 ± 2.6	10.8 ± 3.3
5563853506009853568	8483.796 ± 0.006	9.3 ± 3.9	0.46 ± 0.30	7.9 ± 3.2	6.4 ± 1.3	8.1 ± 1.6
5637175400984142336	8522.027 ± 0.009	25.4 ± 28.7	0.11 ± 0.11	5.6 ± 2.6	4.3 ± 2.1	5.4 ± 2.6
5661194163772723072	8525.277 ± 0.005	4.9 ± 2.4	0.29 ± 0.30	2.6 ± 2.0	2.6 ± 0.6	3.2 ± 0.8
5661194163772723072	8563.632 ± 0.005	14.3 ± 11.5	0.12 ± 0.13	4.0 ± 1.7	2.7 ± 1.1	3.4 ± 1.4
5884382654716110848	8631.969	–	–	–	1.2 ± 1.0	1.6 ± 1.2
5884382654716110848	8649.319	–	–	–	0.6 ± 0.5	0.8 ± 0.7
5891504088488622208	8607.471 ± 0.009	31.0 ± 27.6	0.15 ± 0.13	9.3 ± 3.8	7.0 ± 3.4	8.8 ± 4.2
5891504088488622208	8609.402 ± 0.006	15.2 ± 7.8	0.31 ± 0.20	9.6 ± 3.2	7.3 ± 2.3	9.3 ± 2.9
599891555546067072	8497.566 ± 0.006	7.4 ± 5.6	0.16 ± 0.18	2.4 ± 1.3	1.4 ± 0.8	1.7 ± 1.0
599891555546067072	8499.771 ± 0.006	19.3 ± 19.2	0.09 ± 0.10	3.8 ± 1.2	2.5 ± 0.7	3.2 ± 0.9
599891555546067072	8509.263 ± 0.000	4.8 ± 0.8	1.12 ± 0.36	9.8 ± 1.6	3.8 ± 0.6	4.8 ± 0.7
6135947032490329472	8590.261 ± 0.000	8.2 ± 0.2	2.39 ± 0.05	35.6 ± 0.2	76.1 ± 0.2	95.9 ± 0.3
6135947032490329472	8615.856 ± 0.006	3.8 ± 1.5	0.32 ± 0.27	2.1 ± 1.5	1.1 ± 0.2	1.4 ± 0.3
6135947032490329472	8622.737 ± 0.009	16.0 ± 20.2	0.02 ± 0.03	0.7 ± 0.3	0.5 ± 0.3	0.7 ± 0.3
6525046188759705728	8376.547 ± 0.007	17.6 ± 14.7	0.14 ± 0.14	5.5 ± 2.0	4.1 ± 1.7	5.2 ± 2.2
6783123184369906816	8327.900 ± 0.006	7.8 ± 5.5	0.20 ± 0.20	3.2 ± 1.7	1.4 ± 1.3	1.7 ± 1.6
6783123184369906816	8345.119 ± 0.001	9.7 ± 7.3	0.33 ± 0.26	6.2 ± 1.2	4.1 ± 1.0	5.2 ± 1.2
6783123184369906816	8345.118 ± 0.001	8.7 ± 5.9	0.39 ± 0.27	6.4 ± 1.3	4.1 ± 0.9	5.2 ± 1.2
697274883805771776	8878.651 ± 0.005	10.8 ± 1.6	2.83 ± 0.91	56.4 ± 14.0	56.5 ± 2.2	71.2 ± 2.8
706729107552444672	8873.242 ± 0.005	31.2 ± 15.0	0.22 ± 0.10	12.9 ± 2.9	11.4 ± 2.4	14.4 ± 3.0
901941452829250560	8846.097 ± 0.000	6.2 ± 1.0	1.45 ± 0.36	16.5 ± 1.7	7.2 ± 1.0	9.1 ± 1.2
901941452829250560	8860.962 ± 0.006	8.8 ± 3.6	0.36 ± 0.23	5.8 ± 2.4	4.2 ± 0.9	5.3 ± 1.1
901941452829250560	8865.911 ± 0.216	36.0 ± 67.2	0.04 ± 0.06	2.9 ± 1.9	3.0 ± 1.3	3.8 ± 1.6
947463811200288512	8852.468 ± 0.001	5.9 ± 0.7	1.85 ± 0.38	20.0 ± 2.5	52.7 ± 1.4	66.4 ± 1.7
947463811200288512	8867.782	–	–	–	5.5 ± 5.5	6.9 ± 6.9
1123855296251645824	9031.140 ± 0.001	16.3 ± 9.2	0.45 ± 0.29	14.1 ± 2.3	10.2 ± 2.1	12.8 ± 2.7
1125848440251239424	9033.948	–	–	–	7.4 ± 4.7	9.3 ± 5.9
1361972479325240960	9024.755 ± 0.007	18.2 ± 7.3	0.50 ± 0.30	18.0 ± 7.0	19.7 ± 3.4	24.8 ± 4.3

Appendix C: Comoving pairs

We present the parameters of 19 comoving pair candidates in Table C.1.

Table C.1. Comoving pair candidates from *Gaia* DR2

target Gaia DR2 source ID	companion Gaia DR2 source ID	separation [au]	kinematic age [Gyr]	comment
779689533779300736	779689606794219136	390	-	M6.5Ve
794031395948224640	794031395950867968	240	-	
1412377317863375488	1412377493957462784	2060	3.7 ± 3.3	K3V with v_{rad}
1688578285187648128	1688578280891900416	180	-	M3.5V
2088442248714858368	2088442248714858624	90	-	
2117179153332367232	2117179153330391040	830	-	brown dwarf candidate
2310240437249834496	2310240372825841280	750	-	
3732207661169873792	3732206772112073984	6190	6.1 ± 3.4	K2 with v_{rad}
3999432971480096640	3999433452516434560	5050	5.6 ± 3.0	M3V with v_{rad}
4126080699371400064	4126080699385397888	440	-	
4293315765165489536	4293318823182081408	440	4.0 ± 3.3	M3V with v_{rad}
4339417394313320192	4339465360508118912	1940	5.4 ± 3.3	M3.5V with v_{rad}
5070595856596619136	5070595856597335040	510	1.8 ± 3.0	M with v_{rad}
5627865354993448960	5627865694299883008	9920	1.6 ± 3.0	G9V with v_{rad}
5627865354993448960	5627865698590777728	9970	-	
5809399363316630912	5809399363316632064	70	-	
6357834388848708224	6357835694518769408	6220	0.8 ± 2.6	G0V with v_{rad}
6503514658710993664	6503514697366717568	1810	-	M4
6645843007247800704	6645843007249648768	780	5.8 ± 3.4	M2 with v_{rad}
6783123184369906816	6783123184369906944	60	-	